Preprints (www.preprints.org) | NOT PEER-REVIEWED | Posted: 15 March 2021 doi:10.20944/preprints202103.0393.v1

Article

Discrete element method modeling for the failure analysis of dry mono-size coke aggregates

Alireza Sadeghi-Chahardeh [1], Roozbeh Mollaabbasi [1], Donald Picard [2], Seyed Mohammad Taghavi [3] and Houshang Alamdari [1,*]

[1] Aluminum Research Centre–REGAL, Mining, Material, and Metallurgy Engineering Department, Université Laval, 1065 Avenue de la Médecine, Québec, QC G1V 0A6, CANADA; alireza.sadeghi-chahardeh.1@ulaval.ca (A.S.C.), roozbeh.mollaabbasi.1@ulaval.ca (R.M.), houshang.alamdari@gmn.ulaval.ca (H.A.)
[2] Aluminum Research Centre–REGAL, Civil Engineering Department, Université Laval , Québec, QC G1V 0A6, CANADA; Donald.Picard@gci.ulaval.ca (D.P.)
[3] Chemical Engineering Department, Université Laval, 1065 Avenue de la Médecine, Québec, QC G1V 0A6, CANADA; seyed-mohammad.taghavi@gch.ulaval.ca (S.M.T.)
* Correspondence: houshang.alamdari@gmn.ulaval.ca

Abstract: An in-depth study of the failure of granular materials, which is known as a mechanism to generate defects, can reveal the facts about the origin of the imperfections such as cracks in the carbon anodes. The initiation and propagation of the cracks in the carbon anode, especially the horizontal cracks below the stub-holes, reduce the anode efficiency during the electrolysis process. In order to avoid the formation of cracks in the carbon anodes, the failure analysis of coke aggregates can be employed to determine the appropriate recipe and operating conditions. In this paper, it will be shown that a particular failure mode can be responsible for the crack generation in the carbon anodes. The second-order work criterion is employed to analyze the failure of the coke aggregate specimens and the relationships between the second-order work, the kinetic energy, and the instability of the granular material are investigated. In addition, the coke aggregates are modeled by exploiting the discrete element method (DEM) to reveal the micro-mechanical behavior of the dry coke aggregates during the compaction process. The optimal number of particles required for the failure analysis in the DEM simulations is determined. The effects of the confining pressure and the strain rate as two important compaction process parameters on the failure are studied. The results reveal that increasing the confining pressure enhances the probability of the diffusing mode of the failure in the specimen. On the other hand, the increase of strain rate augments the chance of the strain localization mode of the failure in the specimen.

Keywords: Carbon anode production, Crack generation, Discrete element method, Failure analysis, Second-order work criterion, Strain localization

1. Introduction

Carbon anodes are part of the chemical reaction of the alumina reduction and are consumed during the Hall-Héroult electrolysis process. The mechanical and chemical qualities of the carbon anodes directly affect the technological, economical, and environmental aspects of the aluminum production process. The carbon anode production accounts for 17 % of the total cost of the aluminum smelting [1]. To produce one ton of aluminum, theoretically, 334 kg of carbon would be required. However, in practice, the required carbon is higher and roughly about 415 kg per ton of aluminum [2]. The carbon anodes are composed of three major parts, i.e. the calcined petroleum coke (65 wt. %), the recycled anode (butt, 20 wt. %), and the coal tar pitch (15 wt. %). Initially, the coke particles are crushed and sieved to the required size distribution, and they are mixed with the granulated recycled butts. The dry aggregates are then heated to about 160 °C and mixed with the coal tar pitch at 150–180 °C. The coal tar pitch binds the coke and butt particles. The obtained mixture is called the anode paste. The anode paste goes through the vibro-compaction or the pressing process to form the green anode blocks. To improve the mechanical strength and electrical conductivity, the green anodes are baked at a temperature of 1100 °C. Then, the obtained baked anodes can be used as electrodes in the aluminum smelters [3].

© 2021 by the author(s). Distributed under a Creative Commons CC BY license.

Preprints (www.preprints.org) | NOT PEER-REVIEWED | Posted: 15 March 2021 doi:10.20944/preprints202103.0393.v1

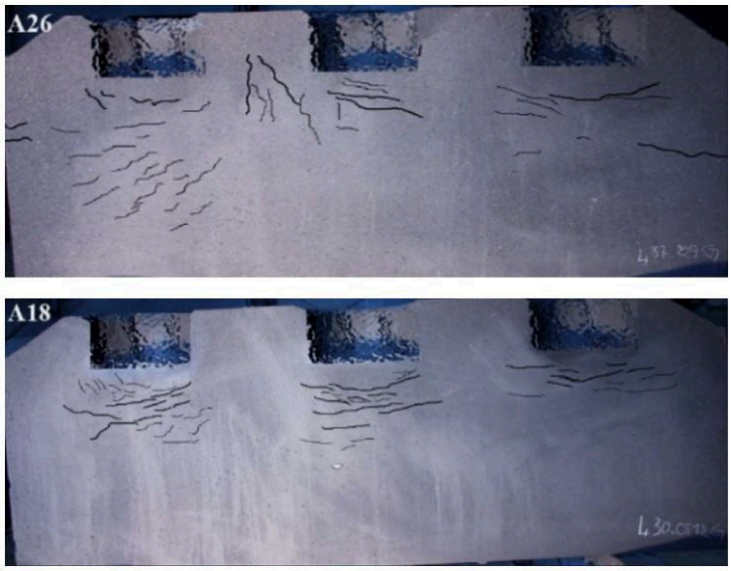

Figure 1. Images of cuts made on baked carbon anodes which are manufactured at the Alcoa Deschambault Québec (ADQ) smelter [4]. (The size of cracks in these images has been virtually enlarge for a clearer visual appreciation).

High mechanical strength and electrical conductivity, homogeneity, as well as low reactivity towards carbon dioxide and air, are the important quality indices of the carbon anodes [5]. The main parameters determining the final anode quality are categorized into two essential groups; the material properties and the process parameters [6]. The variations in the properties of the raw materials are considered as one of the most significant challenges in the anode manufacturing industry. This quality variation is due to the fact that the raw materials come from different sources. When the material properties are changed, the paste formation and the process parameters including the mixing variables and the compaction parameters should be re-adjusted in such a way to compensate for the effects of the variations and to keep the anode quality consistent. Moreover, the sufficient mixing power and time, the optimized speed of the vibro-compaction, and the confining pressures, as well as the proper temperature, are the most important process parameters determining the mixing effectiveness and the anode quality. An efficient mixing results in a homogeneous distribution of the coke and the coal tar pitch, and lower porosity in the paste that improves the anode characteristics such as the density and the thermal shock resistance [5]. In addition, any changes in either the speed and load of pressing forming or the frequency and dead-weight of the vibro-compaction process influence the homogeneity of the density of the green anodes, as well as the quality of the baked anodes [7]. Similarly, the higher baking temperature leads to larger crystallite sizes and a more homogeneous structure of the pitch-coke, which reduces the electrical resistivity and the consumption rate of the carbon anodes [8].

Any defects such as the internal and the external cracks and the density distribution affect the carbon anode consumption rate and remarkably increase the process costs [7]. The presence of the cracks reduces the mechanical strength and the electrical conductivity of the baked carbon anode, thereby reducing the life of the carbon anode, disrupting the cell stability, and increasing the greenhouse gas emissions [6]. Given that all the steps of anode production are done at high temperatures and the components of the anode paste are opaque, it is not easy to investigate the origins of the cracks. The cracks can be formed during the green carbon anode preparation, as well as during the baking process [9,10]. Many researchers have attempted to discover the reasons for the formation of the cracks in the carbon anodes. Menard [11] attributed the generation of the cracks during the green

Preprints (www.preprints.org) | NOT PEER-REVIEWED | Posted: 15 March 2021 doi:10.20944/preprints202103.0393.v1

anode formation to two factors, trapping compressed air in the anode paste during the formation and inhomogeneous distribution of the binder, which causes adhesion between the coke particles. Moreover, Amrani et al. [12] ascribed the crack formation to the releasing of the volatiles from the coal-tar pitch during the baking process, which can create pressure inside the carbon anodes.

Three major types of the cracks can develop in the carbon anodes: corner, vertical, and horizontal cracks [13]. The corner cracks predominantly appear after the anode is set into the electrolysis cell due to the thermal shock [14]. The vertical cracks are created mainly during the baking process. The high temperature gradient inside the carbon anode due to the high heating rate provides the tensile stresses required to create the vertical cracks [8]. The horizontal cracks of the anodes are the most detrimental to the electrolysis operation [13]. Under normal circumstances, the stresses caused by the thermal shock cannot generate these types of cracks [13]. These defects should already appear as small horizontal cracks that are likely to occur during the formation process [13]. Boubaker et al. [4] reported a kind of the horizontal cracks below the stub-holes of the baked carbon anodes. In Figure 1, the baked carbon anodes are cut from the middle and shows the horizontal cracks under the stub-holes. Although these cracks are not present in all the anodes, they are accidentally observed beneath the stub-holes. In the compaction process, however, the compression stresses around the stub-holes appear to be higher than in other parts of the carbon anode. Hence, It seems strange to have these types of cracks where they are probably denser than elsewhere in the anode [15]. On the other hand, because these cracks are the opening type, the tensile stresses perpendicular to the direction of the crack growth is required to generate them [16]. However, the origin of these tensile stresses beneath the stub-hole is not known [4].

Many investigations have been conducted to find the cause of the formation of the cracks [15,17]. Due to the high temperature of the forming process and the opacity of the carbon anode paste, the experimental investigations are not easily performed. Chaouki et al. [15] proposed a constitutive law to simulate the anode paste during the compaction process. Although this model can reveal the density gradient due to the stub-hole, it is not capable of demonstrating the formation of the horizontal cracks below the stub-hole [15,17]. This limitation stems from the fact that the granularity nature of the anode paste cannot be taken into account by phenomenological models such as finite element methods [18]. On the other hand, several attempts have been made to investigate the behavior of anode paste using the discrete element method (DEM), which considers grains as the basic element from which the mechanical behavior of granular materials originates [6,19]. Despite the fact that modeling anode paste with all its complexities, including different size distribution, particle shape, solid-fluid interaction, and coal-tar pitch dependence on temperature, is a challenging task, DEM has shown that it is able to simulate successfully some properties of the anode coke aggregates such as the bulk density [20] and the electrical resistivity [21]. However, investigating the causes of the horizontal cracks under stub-holes requires more in-depth analysis. Hence, a comprehensive study of the distinct behaviors of granular materials subjected to compression loading conditions can shed light on the hidden truth of this problem.

The granular materials are generally defined as those composed of the smaller particles, and in our case, those whose mechanical behavior is governed by the interaction between the particles [18]. When the granular material is exposed to a compression load, it reaches a stress state wherein it is no longer able to sustain any deviatoric load increment. At such a limited stress state, if an additional load is imposed the state of the material changes suddenly with the occurrence of large deformations, cracks, fragmentation, etc [22]. This circumstance, which is associated with a sudden decrease in the number of grain contacts, is called failure [23]. The sudden reduction in the grain contacts leads to a significant increase in the number of degrees of freedom which implies the possibility of rapid relative displacements between the grains. Due to these rapid relative displacements between the grains, the failure is a physical phenomenon that can be regarded as a state

Preprints (www.preprints.org) | NOT PEER-REVIEWED | Posted: 15 March 2021 doi:10.20944/preprints202103.0393.v1

from which a transition from a quasi-static regime to a dynamical regime is possible under certain constant loading parameters [24]. For the materials with an associative flow rule, as it is generally assumed for metals, the symmetry of the elasto-plastic tensor leads to the compelling fact that the failure occurs in the plastic limit condition. However, for granular materials, which are known to have non-associated flow rules and consequently non-symmetry in the elasto-plastic tensor, the failure can be met before the plastic limit condition (Mohr-Coulomb criterion) [25]. The mathematical interpretation of the failure is usually attributed to the existence of a limit load that cannot be exceeded for a given mechanical system under some boundary and initial conditions [26].

The failure in the granular materials is initiated by the instability of these materials [27]. The instability can be either geometric such as structural instability [28], or material such as constitutive behavior and force chains buckling [25,29]. The geometric instability is associated with the tendency of the configuration to pass from one deformation pattern to another [28]. For instance, the critical condition of a long, slender column that is axially loaded is a state of transition from pure compression to a combination of compression and bending. Therefore, this type of instability is a function of the geometry of the specimen and its loading [30]. On the other hand, material instability is defined as a property of the material that converts an initially homogeneous deformation field into a heterogeneous deformation field [31]. The material instability is related to the size of the materially intrinsic length scales, which is called microstructure, and the magnitudes of the length scale of the initial perturbations [29,31]. For example, local buckling of particle force chains is considered as a material instability [29,32].

The material instability leads to the loss of uniqueness of the solution of the underlying governing equations, hence to a bifurcation problem [33]. When a mechanical state belongs within the bifurcation domain, failure is possible depending on the loading parameters, loading history, disturbances, and imperfections in the system [22]. Due to this dependence on small perturbations, the failure can also be viewed as an instability phenomenon in the basic Lyapunov sense [34]. Lyapunov's definition of stability expresses that for a given rate-independent material, a stress-strain state for a given strain history is called stable if any small change of any admissible loading leads to a small change of the response. However, the main question that comes to mind is, according to Lyapunov's definition of stability, how can be shown a stress-strain state is unstable strictly inside the plastic limit surface?

Two concepts of failure are built around the above-mentioned question of describing the failure. The first one is the notion of controllability [35] and the second one is the sustainability of equilibrium states [36]. Nova [35] proceeded by defining controllability as the ability of a material (or a model) to provide one and only one (existence and uniqueness) response to any loading path for which some strain components and the other stress components are prescribed. According to [35], granular materials lose their controllability at a certain stress level and after that point, the specimen does not give rise to a unique material response under any arbitrary incremental loading program. At this point, the stiffness tensor is no longer positive definite. It has been shown that as soon as the stiffness tensor becomes positive semi-definite, there is a particular program that leads to infinite solutions and unconditional controllability is lost [37]. The concept of controllability is an interpretation of the Lyapunov definition of stability. As the notion of controllability applies to a given loading program, therefore, this is not an intrinsic characteristic of the mechanical state of the system [35]. On the other hand, another interpretation of the Lyapunov definition of stability is about the sustainability of the mechanical state of the system. The sustainability of equilibrium states defined as an ability of a mechanical system loaded with specific control parameters to evolve toward another mechanical state from a given equilibrium state, with no change in the control parameters [36]. If this is true, the equilibrium state of the material is reputed unsustainable, and the subsequent loss of sustainability corresponds to a proper bifurcation mode. From a mechanical point of

Preprints (www.preprints.org) | NOT PEER-REVIEWED | Posted: 15 March 2021 doi:10.20944/preprints202103.0393.v1

view, it means that a system that is initially in equilibrium can generate kinetic energy spontaneously and without any external disturbances [26,36].

Due to the difficulty with Lyapunov definition of stability, there was a need for a related manageable criterion of failure for the practical use in the investigation of the granular materials [38,39]. To compensate for this issue, Hill's second-order work criterion of stability has been introduced. According to Hill [40], a stress-strain state is unstable if there exists one loading direction which can be pursued in an infinitesimal manner without any input of the energy from an external source. Although Hill's criterion and Lyapunov's definition of stability are not related in a general manner [41], the concepts of controllability and sustainability are equivalent to the Hill's criterion in the classical elasto-plasticity [35] and the failure of granular materials [39,42]. Therefore, in spite of the fact that this criterion does not specify the mode of material failure [24], it can predict the necessary conditions for the occurrence of a failure in the granular materials.

Various modes of failure in granular materials have been observed in practice. Thanks to experimental observations, there are two broad classes of failure modes that arise in the granular materials due to some instabilities [43]. In the granular materials, excluding flutter instabilities, two material failure modes are of interest: localized and diffuse failure modes. At a material point scale, the localized failure mode corresponds to a transition from a homogeneous strain pattern to an inhomogeneous one, characterized by the appearance of a system of bands in which strains concentrate [44]. These narrow zones where deformation is concentrated are called localized bands. Depending on the loading path and their kinematic attributes, shear, dilation, or compaction bands may be developed [45]. While the shear bands are predominated by shearing, the dilation and compaction bands are formed primarily by volumetric deformation and they are characterized by local volume expansion and local volume reduction, respectively [45]. The strain localization of the granular materials has been studied by many researchers through theoretical [44,46–48], experimental [49–54], and numerical methods [55–58]. There have been attempts to simulate the phenomenon of the strain localization in the granular material, especially in the sand samples, based on either continuum mechanics by using the finite element method (FEM) [55,56] or micro-mechanics by using the discrete element methods (DEM) [53,57]. The finite element methods (FEM) require the constitutive relation of the material, while there are no reliable constitutive laws that can accurately predict the behavior of the granular materials [59]. It should be noted that the constitutive laws derived from the classical continuum mechanics do not take into account the dimensions of the granular elements [18,60]. Consequently, these constitutive laws suffer from pathological mesh-dependency when they are employed in the failure analyses [61,62]. However, the discrete element method can provide applicable equipment for considering the internal length scale of the granular material without involving the sophisticated mathematics of the non-classical continuum mechanics [63]. In addition, a combination of the latter two methods, called multi-scale methods, is also used to model the strain localization in the granular materials, which benefits from both FEM and DEM [18,58,62,64,65].

On the contrary, the diffusing failure mode corresponds to a homogeneous occurrence of the failure in which no visible pattern of localization exists [66]. A chaotic, unstructured strain field dominates [41]. This failure mode can be observed mostly in the loose sand specimens for classical tests [67]. Diffusing failure does not occur in the dense sand under undrained conditions [68]. This is the case, for instance, for the isochoric triaxial test carried out on a loose sand specimen. At the deviatoric peak, an infinitesimal loading disturbance is sufficient to provoke the abrupt collapse of the specimen without any localization pattern [38,66]. While the localized failure is predicted by the vanishing values of the determinant of the acoustic tensor [46], known as classical bifurcation analysis, the second-order work criterion is mostly used as a proper indicator of the diffuse failure mode [66]. Although there are differences in the kinematics properties of the two failure modes, [69] showed that both localized and diffuse failure can be predicted through the classical bifurcation analysis. Despite the difficulty in finding a proper constitutive law that describes the

Preprints (www.preprints.org) | NOT PEER-REVIEWED | Posted: 15 March 2021 doi:10.20944/preprints202103.0393.v1

granular material's behavior, the bifurcation analysis has been used widely to predict failure in the sands [56,70], the rocks [71], and the fluid-saturated granular soils [72,73]. Moreover, it has been shown that the second-order work criterion is capable to detect both the diffuse and the localized failure modes [24]. This criterion, unlike the classical bifurcation analysis, does not require necessarily a constitutive law to predict failure [74].

Comprehension of failure as a mechanism to generate defects in granular material can reveal the facts about the origin of the imperfections such as cracks in the granular materials (e.g. see [45,75] and the references cited in them). In geology, the localized bands are recognized as the main mechanism of fault formation in sandstone which precedes the formation of the larger faults [76,77]. As these localized bands are usually associated with porosity reduction, they may provide a natural barrier to fluid flows and form hydrocarbon reservoirs and aquifers [78,79]. Another type of localized bands, called compaction bands, is formed by the accommodation of pure compaction (with little or no shear) in the tabular zone perpendicular to the maximum compression direction in the sandstone or the sedimentary rocks [80–82]. There are compelling evidence for the existence and the formation of compaction bands in the granular materials that are exposed to the compressive stress states both in the laboratory and in the theory [82]. Although compaction bands were first recognized in the sandstone [80], similar phenomena appear to be common in the other porous materials [83]. For instance, Bastawros et al. [84] were able to illustrate the formation of the compaction bands in a cellular aluminum alloy upon axial compression through a digital image correlation procedure. Similar observations had been reported for steel foams [85] and polycarbonate honeycombs [86] in which inherent pore collapse has mainly caused the formation of the compaction bands.

The characteristics of the compaction bands, such as being perpendicular to the maximum principal compression direction, as well as the similarity in the way of loading, which is mainly compressive, have led us to the idea that the horizontal cracks beneath the stub-holes in the carbon anodes can be generated by these bands. Figure 2 shows how internal tensile stresses could generate inside the carbon anode even in the absence of an external load. When the compressive stresses are applied to the carbon anode paste, due to the stub-hole shape effect, the areas below the stub-holes subject to more compaction than their neighboring areas (Figure 2 (a)). It is assumed that this additional compression can cause the compressive strain to accumulate in a narrow rectangular region, resulting in a compression band (dashed rectangle in Figure 2 (b)). After removing the external load from the material, due to the viscoelastic properties of the carbon anode paste, the compression accumulated in the compaction bands causes residual tensile stresses in the stub-hole region, as well as residual compressive stresses in the neighboring areas (Figure 2 (c)). Accordingly, the compaction bands could be responsible for the tensile stresses which are required for the generation of these type of cracks. This phenomenon is similar to the inclusion problem in the elastic media described by Eshelby [87]. Although many researchers used an analogous method to predict the initiating of the compaction bands in the porous rocks [81,88–90], the factors influencing the various manifestations of the compression bands are still unknown [82]. Therefore, understanding the failure behavior of the granular materials is of great importance to find the mysterious phenomena of compaction band formation. In addition, due to the fact that detection of the compaction bands is difficult in either the field or the laboratory [82], it is possible that compaction bands are present in virtually all the carbon anodes (even in the cases where there are no horizontal cracks). Although some parameters, such as thermal shocks or shrinkage of the coal-tar pitch during the baking process, affect the formation of the cracks in the carbon anodes, the compaction bands are a mechanism that can create a susceptible region under the stub-holes to generate the horizontal cracks. Therefore, it is necessary to determine the factors of the physical conditions and the material characteristics associated with the formation of the compaction bands in the case of a systematic investigation.

As aforementioned, the existence of compaction bands in the visco-elastic anode paste creates a susceptible area for the horizontal crack formation. While the temperature

Preprints (www.preprints.org) | NOT PEER-REVIEWED | Posted: 15 March 2021 doi:10.20944/preprints202103.0393.v1

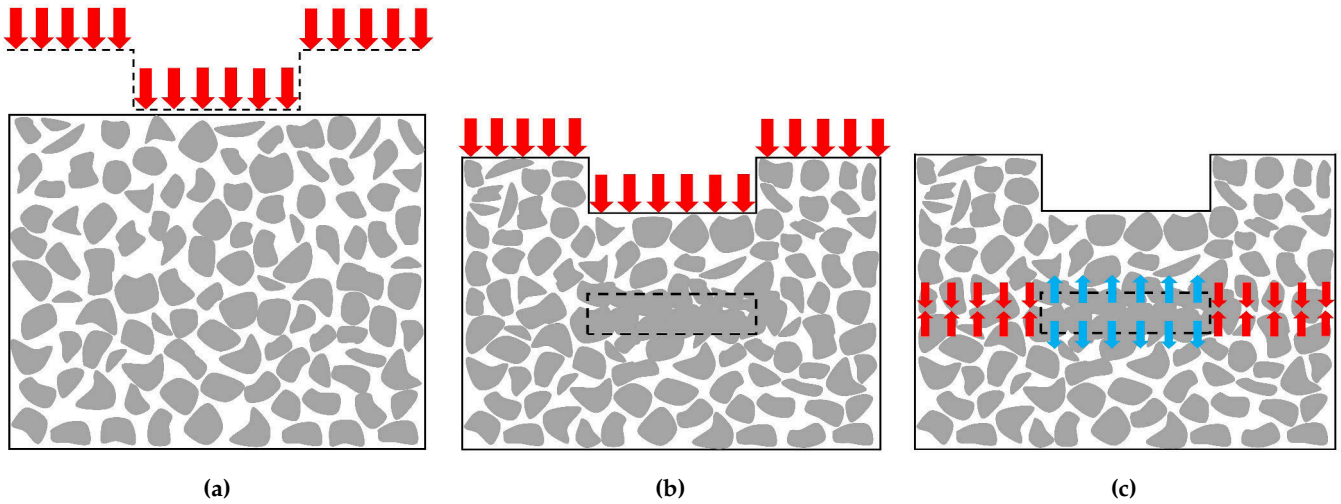

Figure 2. Generation of the residual tensile stresses due to compaction band formation. (a) The carbon anode paste before the compaction process. (b) The carbon anode paste during the compaction process and the formation of the compaction band (dashed rectangle). (c) Creating residual stresses in the absence of the external pressure. (The red arrows indicate the compression stresses and the blue ones show the tensile stresses).

and coal-tar pitch content affect the viscous part of the anode paste, the coke particle characteristics influence the elastic part of the anode paste behavior [5]. Therefore, it seems reasonable to consider only the coke particles for the failure analysis. In addition, the coarse coke particles have been shown to form a skeleton that controls the main mechanical behavior of coke aggregates [91]. Hence, for the sake of simplicity, we will consider the coarse coke particles with spherical shape for our investigations. Accordingly, in this paper, the second-order work criterion for the failure of the granular material will be reviewed and the influence of failure on the kinetic energy of the system will be explained in Section 2. In addition, the ability of the second-order work criterion in diagnosing the failure of the granular material will be discussed. In Section 3, the concept of the discrete element method will be presented. The criteria for choosing the proper representative volume element (RVE) will be studied. In Section 4, the strain localization analysis is presented based on the second-order work criterion and the evolution of the mode of the localized bands will be discussed. The most salient results of this work will be summarized and discussed in Section 5.

Throughout this paper, the material time derivatives of any variable ψ will be distinguished by denoting $\frac{D\psi}{Dt}$ and the particulate time derivative of ψ defined as $\dot{\psi}$. The first-order tensors (vectors) and the second-order tensors, respectively, denoted by lower-case bold Latin ($\mathbf{v}$) and upper-case bold Latin ($\mathbf{F}$). Moreover, the subscript 3 throughout the paper indicates the axial direction, while the subscripts 1 and 2 were designated as lateral directions.

2. Second-order work criterion

In mechanical problems, where the existence of a potential energy function can be assumed, with some particular hypotheses on conservative and dissipative forces, stability is ensured if this potential function has a strict minimum. Due to complex dissipative phenomena, a potential energy function does not exist in mechanics problems involving granular media [38]. Therefore, the material instabilities thus cannot be studied through the analysis of potential energy function. In other words, these instabilities are linked to the inherent deformation mechanisms of the granular material and do not depend on the potential energy. In addition, the theoretical investigations, the numerical analyses, and the experimental results highlight that the concept of failure is related to the development of kinetic energy [26,68,92,93]. As a consequence, it is necessary to have criteria that relate the kinetic energy of granular material to the control parameters (such as strain or stress

Preprints (www.preprints.org) | NOT PEER-REVIEWED | Posted: 15 March 2021 doi:10.20944/preprints202103.0393.v1

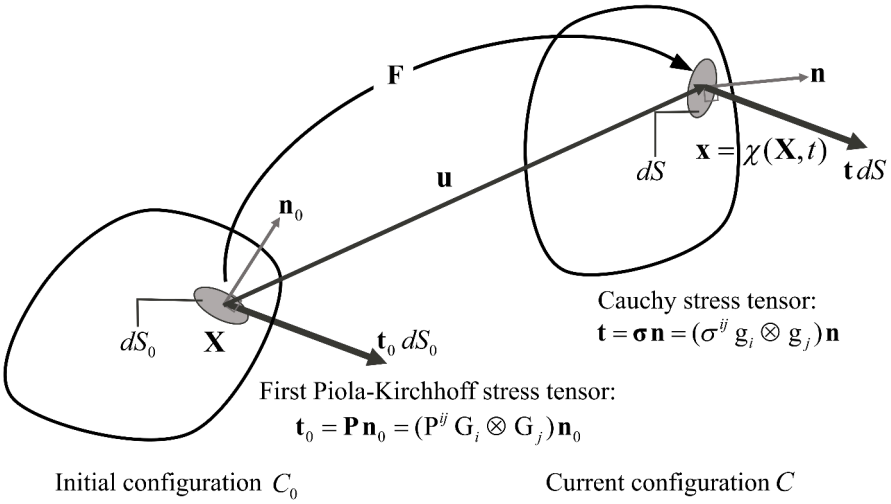

Figure 3. Definition of the First Piola-Kirchhoff stress tensor and Cauchy stress tensor and transformation of a material system.

at the boundaries). Hence, the issue of stability will be investigated using Hill's second-order work criterion [40]. This sufficient condition of failure states that a stress-strain state is stable if, for all ($\delta\mathbf{P}$, $\delta\mathbf{F}$) in the semi-Lagrangian formulation or ($\delta\boldsymbol{\sigma}$, $\delta\boldsymbol{\epsilon}$) in Eulerian formulation (by assuming small deformations and neglecting geometrical aspects) linked by the constitutive relation, the second-order work is strictly positive [94]:

$$\begin{aligned} d^2W &= \iiint_{V_0} \delta P_{ij}\, \delta F_{ij}\, dV_0 > 0 \quad \text{(semi-Lagrangian expression)}\,, \\ d^2W &= \iiint_{V} \delta\sigma_{ij}\, \delta\epsilon_{ij}\, dV > 0 \quad \text{(Eulerian expression)}\,, \end{aligned} \tag{1}$$

where P_{ij} is the first Piola-Kirchhoff stress tensor, F_{ij} the general term of the deformation gradient tensor, σ_{ij} the Cauchy stress tensor and, and ϵ_{ij} is the strain tensor. Thus, according to Hill, a stress-strain state is unstable if at least one loading direction exists that can be pursued in an infinitesimal manner without any input of energy from the outside. It is worth noting that the vanishing of the second-order work implies the loss of controllability of the loading program, independently of the constitutive relations has been proved, independently of the constitutive relations [37]. Although this sufficient condition is not based on thermodynamic principles, it still remains a valuable tool for investigating potential instabilities [38]. The nullity of the second-order work criterion is a powerful tool to describe any kind of quasi-static material instability by taking into account that flutter instabilities are dynamic.

2.1. kinetic energy of the granular system and external and internal second-order work

An attempt for the definition of the failure in the granular material was made in the previous section, and this related to a transition (bifurcation) from a quasi-static regime toward a dynamic one. In this section, the mathematical description of the second-order work criterion is developed and the conditions in which the kinetic energy of the granular material system may increase will be investigated. For this purpose, a system consisting of granular material, with a volume, V_0, and a surface boundary, S_0, initially in a configuration, C_0, is considered. With a loading history, the system is in a current configuration, C, with a volume, V, and the surface boundary, S, in equilibrium under a prescribed external load. Each material point in the volume V_0 is transformed into a material point in the volume V (Figure 3). All the material points in the volume V_0 are displaced along with the deformation of their geometric properties, including the surface vector, the area, and the volume. During this transformation, the material is subjected to a rigid body motion, along

Preprints (www.preprints.org) | NOT PEER-REVIEWED | Posted: 15 March 2021 doi:10.20944/preprints202103.0393.v1

with the pure strain induced by the stretching and the spinning deformations. If large amounts of strain take place, the initial configuration, C_0, will be significantly different from the current configuration, C.

As the Cauchy stress tensor is not objective (in the rigid body transformation, it gives different values), the first Piola-Kirchhoff stress tensor and the conservation of the mechanical energy in the material description are used [95,96]. It should be noted that the first Piola-Kirchhoff stress vector is the vector $t_0(X,t,n_0)$, which is parallel to the Cauchy stress $t(x,t,n)$, but measures the force per unit undeformed area (see Figure 3). The balance of the kinetic energy of a system with neglecting the body force in the material description (configuration C_0) can be derived as [97]:

$$\frac{D}{Dt}\mathcal{K}(t) = \mathcal{P}_{ext}(t) - \mathcal{P}_{int}(t)\,, \tag{2}$$

or

$$\frac{D}{Dt}\iiint_{V_0}\left(\frac{1}{2}\rho_0\mathbf{v}\cdot\mathbf{v}\right)dV_0 = \iint_{S_0}\mathbf{P}\mathbf{n}_0\cdot\mathbf{v}dS_0 - \iiint_{V_0}\mathbf{P}:\dot{\mathbf{F}}dV_0\,. \tag{3}$$

Equation (3), expresses that the rate of change of the kinetic energy, $\mathcal{K}(t)$, is equal to the difference between the power of the external forces, $\mathcal{P}_{ext}(t)$, and the power of the stresses, $\mathcal{P}_{int}(t)$. The stress power, $\mathbf{P}:\dot{\mathbf{F}}$, given in term of the first Piola-Kirchhoff stress tensor $\mathbf{P} = J\sigma\mathbf{F}^{-\mathbf{T}}$ and the deformation gradient $\mathbf{F}$. Note that the stress power $\mathbf{P}:\dot{\mathbf{F}}$ refers to the unit undeformed volume. By taking the time derivative of Equation (3) yields:

$$\frac{D^2}{Dt^2}\iiint_{V_0}\left(\frac{1}{2}\rho_0\mathbf{v}\cdot\mathbf{v}\right)dV_0 = \iint_{S_0}\left(\dot{\mathbf{P}}\mathbf{n}_0\cdot\mathbf{v} + \mathbf{P}\mathbf{n}_0\cdot\dot{\mathbf{v}}\right)dS_0 - \iiint_{V_0}\left(\dot{\mathbf{P}}:\dot{\mathbf{F}} + \mathbf{P}:\ddot{\mathbf{F}}\right)dV_0\,. \tag{4}$$

Furthermore, the two-order Taylor expansion of the kinetic energy reads:

$$\mathcal{K}(t_0+\Delta t) = \mathcal{K}(t_0) + \Delta t\dot{\mathcal{K}}(t_0) + \frac{(\Delta t)^2}{2}\ddot{\mathcal{K}}(t_0) + \text{H.O.T.}\,(\Delta t)\,. \tag{5}$$

Since the velocity of the system in the initial time is equal to zero (quasi-static), the amount of the kinetic energy $\mathcal{K}(t_0)$ and its first time derivative $\dot{\mathcal{K}}(t_0)$ must be equal to zero [93]. In addition, if Δt is considered to be small, then the higher-order terms of Δt (H.O.T. (Δt)) can be ignored. Therefore, by substituting in Equation (5), the kinetic energy in a very small time interval could be predicted as:

$$\mathcal{K}(t_0+\Delta t) = \frac{(\Delta t)^2}{2}\ddot{\mathcal{K}}(t_0)\,. \tag{6}$$

Therefore, by combining Equation (4) and (6), an approximation of the kinetic energy changes in a quasi-static system will be obtained as a function of the external and the internal stress powers.

$$\mathcal{K}(t_0+\Delta t) = \frac{(\Delta t)^2}{2}\left(\overbrace{\iint_{S_0}\left(\dot{\mathbf{P}}\mathbf{n}_0\cdot\mathbf{v} + \mathbf{P}\mathbf{n}_0\cdot\dot{\mathbf{v}}\right)dS_0}^{\dot{\mathcal{P}}_{ext}(t)} - \overbrace{\iiint_{V_0}\left(\dot{\mathbf{P}}:\dot{\mathbf{F}} + \mathbf{P}:\ddot{\mathbf{F}}\right)dV_0}^{\dot{\mathcal{P}}_{int}(t)}\right)\,. \tag{7}$$

Based on Equation (7), the evolution of the kinetic energy of a granular system for every time step can be expressed as the difference between the rate of the external and the internal stress power. It should be noted that this approximation is limited to small time increments [92]. In addition, in Equation (7), it is important to distinguish the stress acting on the boundary and the stress inside the boundary.

Some simplification needed to be taken place for using Equation (7). Hereafter, we particularize the analysis to a cubic representative volume element with dimension

Preprints (www.preprints.org) | NOT PEER-REVIEWED | Posted: 15 March 2021 doi:10.20944/preprints202103.0393.v1

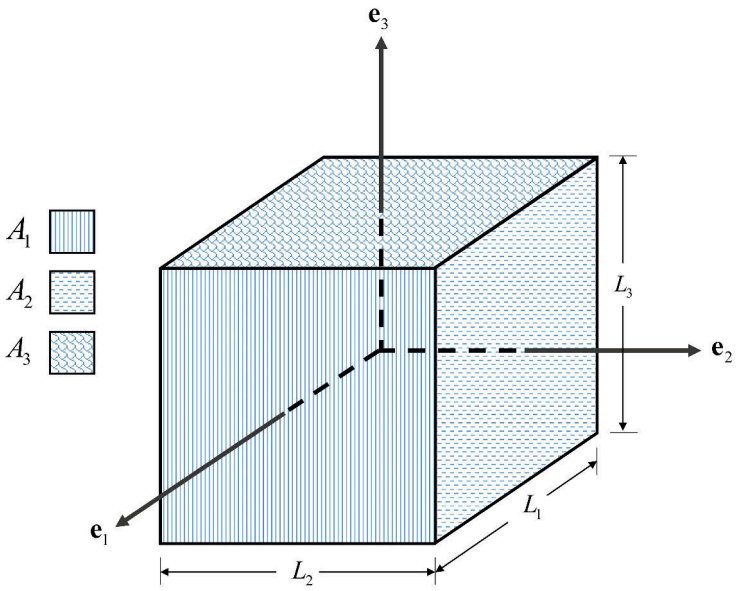

Figure 4. Cubic representative volume element.

$(L_1 \times L_2 \times L_3)$ as defined in Figure 4. The average external stress at the boundaries is determined by summing the contact forces, f, along the boundary, and dividing by the surface area of the rigid boundary for the 3D model. Therefore, the external stress of each side of the boundary, A_i, is equal to:

$$T_i = \frac{f_i}{A_i}\,, \tag{8}$$

where, f_i is the equivalent external force on the side "i" and the A_i is the area of the surface perpendicular to the direction "$\mathbf{e}_i$", as mentioned in Figure 4. The displacement of each side is denoted $u_i = \mathbf{u} \cdot \mathbf{e}_i$. The deformation gradient tensor is defined as $[F_{ij}] = \frac{\partial x_i}{\partial X_j} = 1 + \frac{\partial u_i}{\partial X_j}$. No tangential displacement is assumed to take place. Therefore, the deformation gradient tensor will be in its principal axes. It should be noted that at any material point of the system, both the rate of the first Piola-Kirchhoff stress tensor ($\dot{\mathbf{P}}$) and the rate of the deformation gradient tensor ($\dot{\mathbf{F}}$) are related by the constitutive equation $\dot{P}_{ij} = L_{ijkl}\dot{F}_{ij}$, where the four-order tensor $\mathbf{L}$ is the tangent constitutive tensor for rate-independent materials. Since the first Piola-Kirchhoff stress tensor and deformation gradient tensor are each other's energy conjugate, the first Piola-Kirchhoff stress tensor will be in principle axes as well. Against this background, it could be written:

$$\langle \mathbf{F} \rangle = \begin{bmatrix} \langle F_{11} \rangle & 0 & 0 \\ 0 & \langle F_{22} \rangle & 0 \\ 0 & 0 & \langle F_{33} \rangle \end{bmatrix} \text{ and } \langle \mathbf{P} \rangle = \begin{bmatrix} \langle P_{11} \rangle & 0 & 0 \\ 0 & \langle P_{22} \rangle & 0 \\ 0 & 0 & \langle P_{33} \rangle \end{bmatrix}, \tag{9}$$

where, $\langle Y \rangle$ denotes the mean value of the variable Y over the whole volume V_0, which is defined as:

$$\langle Y \rangle = \frac{1}{V_0} \iiint_{V_0} Y dV_0\,. \tag{10}$$

Preprints (www.preprints.org) | NOT PEER-REVIEWED | Posted: 15 March 2021 doi:10.20944/preprints202103.0393.v1

For the deformation gradient tensor $\langle F_{ii} \rangle = \frac{1}{V_0} \iiint_{V_0} \left(1 + \frac{\partial u_i}{\partial X_j}\right) dV_0$ by virtue of the Green formula, the following hold:

$$\langle F_{ii} \rangle = \frac{1}{V_0} \left(\iiint_{V_0} dV_0 + \iint_{S_0} u_i \mathbf{e}_i dS_0 \right) = 1 + \frac{A_i}{V_0} u_i \,. \tag{11}$$

The detailed mathematical calculations of the first and the second rate of the deformation gradient tensor are provided in Appendix A and B, respectively.

By considering the rate of the external stress power, $\dot{\mathcal{P}}_{ext}(t)$, and the above assumptions, it could be simplified as:

$$\dot{\mathcal{P}}_{ext}(t) = \iint_{S_0} \left[\left(\frac{\partial T_i}{\partial t} \right) \left(\frac{\partial u_i}{\partial t} \right) + T_i \left(\frac{\partial^2 u_i}{\partial t^2} \right) \right] dS_0 \,. \tag{12}$$

Equation (12) can be written as:

$$\dot{\mathcal{P}}_{ext}(t) = \sum_{i=1}^{3} \left(\dot{T}_i \dot{u}_i + T_i \ddot{u}_i \right) A_i \,. \tag{13}$$

due to considering a fixed value of the external stress on each side of the boundary.

In the other hand, the macro-homogeneity assumption makes it possible to invoke the fundamental Hill identity [93], stating that $\langle P_{ij} F_{ij} \rangle = \langle P_{ij} \rangle \langle F_{ij} \rangle$, consequently, by considering the mean value for the first Piola-Kirchhoff stress tensor and the deformation gradient tensor, the rate of the internal stress power, $\dot{\mathcal{P}}_{int}(t)$, could be written as:

$$\dot{\mathcal{P}}_{int}(t) = \iiint_{V_0} \left(\langle \dot{P}_{ij} \rangle \langle \dot{F}_{ij} \rangle + \langle P_{ij} \rangle \langle \ddot{F}_{ij} \rangle \right) dV_0 \,. \tag{14}$$

Combining Equation (11) and Equation (14) gives:

$$\dot{\mathcal{P}}_{int}(t) = \left(\langle \dot{P}_{ij} \rangle \langle \dot{F}_{ij} \rangle + \langle P_{ij} \rangle \langle \ddot{F}_{ij} \rangle \right) V_0 = \sum_{i=1}^{3} \left(\langle \dot{P}_{ii} \rangle \dot{u}_i + \langle P_{ii} \rangle \ddot{u}_i \right) A_i \,. \tag{15}$$

By substituting Equation (13) and (15) in Equation (7), an expression of the kinetic energy as a function of the system's second-order works is obtained:

$$\mathcal{K}(t_0 + \Delta t) = \frac{(\Delta t)^2}{2} \sum_{i=1}^{3} \left[\left(\dot{T}_i - \langle \dot{P}_{ii} \rangle \right) \dot{u}_i + \left(T_i - \langle P_{ii} \rangle \right) \ddot{u}_i \right] A_i \,. \tag{16}$$

The first term of the right-hand side of Equation (16) represents the difference between external and internal second-order work. The second term ($(T_i - \langle P_{ii} \rangle) \ddot{u}_i A_i$) demonstrates the effect of the inertia on the evolution of the kinetic energy. According to Equation (16), the external stress vector (T_i) acting on the boundary of the specimen is equal to the internal stress ($\langle P_{ii} \rangle$) acting within the specimen as long as the system is in the quasi-static evolution, and consequently, the information from the boundary will reveal the material constitutive behavior. Thus, the constitutive response of the specimen can be investigated in that case from the measurable variables T_i and u_i. This information exactly what is evaluated during laboratory tests. On the other hand, when the material failure occurs, the transition from the quasi-static to the dynamic regime, the information which are obtained from the boundary is not the exact information of the material constitutive relations. Hence, the external stresses are not balanced by the internal stresses, and a heterogeneous strain field may develop within the specimen [93]. In addition, when failure occurs, the internal stress will be dropped and according to Equation (16), the terms $\left(\dot{T}_i - \langle \dot{P}_{ii} \rangle \right)$ and $\left(T_i - \langle P_{ii} \rangle \right)$

Preprints (www.preprints.org) | NOT PEER-REVIEWED | Posted: 15 March 2021 doi:10.20944/preprints202103.0393.v1

are greater than zero. Therefore, in this case, leads to $\mathcal{K}(t_0 + \Delta t) > 0$, which describes an outburst in the kinetic energy [92]. Hence, a sudden release in the kinetic energy of the system, could be an indicator of the material failure.

3. DEM simulation

The discontinuous nature of the granular materials causes many phenomena such as the collapse of void space and the buckling of force chains, that cannot be modeled by the phenomenological plasticity methods [63,64]. One possibility to obtain information about the behavior of the granular materials is to perform simulations with the discrete element method (DEM) as proposed by [98]. Because the DEM provides the opportunity to track the motion of every single particle in the grain assembly, it can consider how the microstructures affect the macroscopic properties of the granular material. Therefore, it provides interesting information to describe the mechanisms of the failure in the granular materials.

In this paper, the DEM computations were realized with the open-source software YADE [99]. The particles are assumed to be rigid spheres with a diameter, d_p. The interactions between the particles are simulated in the normal direction to the contact by a linear elastic spring with a stiffness $K_n = 681$ MPa, and in the tangential direction by a linear elastic spring with a stiffness ($K_t/K_n = 0.385$), and the tangential perfect plasticity with a friction angle $\varphi = 18°$ [6]. The normal and the tangential contact forces, f_n and f_t, respectively, are given by:

$$\begin{aligned} f_n &= K_n \delta_n \quad f_n > 0\,, \\ f_t &= K_t \delta_t, \quad f_t \leqslant \tan\varphi f_n\,, \end{aligned} \tag{17}$$

where δ_n is the overlap at the contact point and δ_t is the incremental tangential displacement. At the beginning of a computational time-step, the position of all the elements and the boundaries are known. The contacts are detected by the algorithm according to the known position of the elements and so the magnitude of the possible overlaps between the elements are discovered. The propagated contact forces and momentum on each sphere are then calculated by the interaction law (Equation (17)). After that, the forces are inserted in the law of motion for each particle and the velocity and the acceleration of the particles are calculated. Then, the new sphere positions are calculated by applying Newton's second law of motion. The integration time in Newton's second law and the interaction contact law are both carried out by way of an explicit scheme. The positions of all the particles and the boundaries in the current time-step are determined by the obtained values. This cycle of the calculations is repeated and solved at each time-step, and thus the flow or the deformation of the material is simulated (Figure 5).

Dealing with spherical particles has a great advantage comes from a relatively simple geometry treatment, then two particles will be considered as interacting bodies if the distance between their centers is lower than the sum of their radii. Simulation results presented in this paper were all obtained from two boundary conditions, the periodic and the solid boundary conditions. In the periodic boundary conditions, the particles can go through the boundaries, although the total number of the particles is constant. It is useful for the bulk properties modeling, because it ignores the boundary effect on the behavior of the material [100]. Meanwhile, the solid boundary conditions are used for the failure analysis, which is strictly controlled by the boundary effects [101]. Here, it is assumed that the solid boundaries are frictionless. Therefore, the interaction of the spheres and the walls will be in the normal direction of their contacts. The specimens are generated by randomly inserting grains within a cubic domain (each side is $D_{initial} = 8$ cm long) with the possibility of overlap until a target void ratio is achieved. Then specimens are left to stabilize. Since the time required to complete the calculation depends on the number of particles, determining the optimum number of particles is a challenging part of our work.

Preprints (www.preprints.org) | NOT PEER-REVIEWED | Posted: 15 March 2021 doi:10.20944/preprints202103.0393.v1

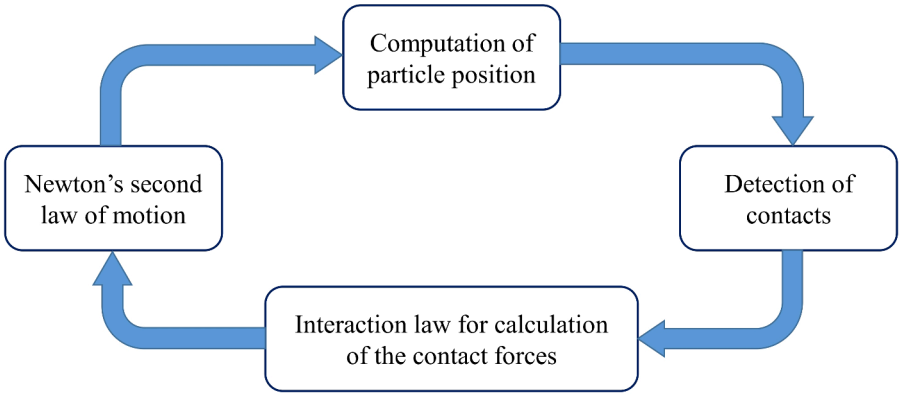

Figure 5. The computation cycle of a DEM model.

Table 1. Coke properties which are used in the DEM model [6].

Radii (mm)	Density (kg/m^3)	Elastic Modulus (MPa)	Poisson ratio	Friction angle (rad)	Damping ratio
1.87	1377	681	0.3	0.31	0.4

3.1. Determination of a proper representative volume element (RVE)

Due to the high computational cost of the DEM simulation, the modeling of the real size of the carbon anode is not practical. Therefore, we need to perform our simulation on the optimum number of particles which could represent the mechanical behavior of the whole material with an acceptable statistical error [102]. Accordingly, six different representative volume elements (RVE) are considered, each of which contains 150, 300, 500, 1000, 2000, 3000, and 4000 particles, respectively. The particle diameter is the same and is equal to 3.74 mm. This is the average diameter of the coarse coke (4-8 US mesh) [19]. The properties of the materials are also given in Table 1. All RVEs are then consolidated to the same initial confining pressure $P_0 = 100$ kPa. Because of the mechanical properties of the RVEs are intended here, their shear responses are examined under a drained conventional triaxial compression loading path. Hence, the load is applied through the displacement-controlled boundaries in the z-direction ($\dot{\epsilon_3} = 0.05\ s^{-1}$), while the lateral boundaries are stress-controlled and maintain a constant value for the lateral stresses ($\sigma_1 = \sigma_2 = 100$ kPa). Various criteria have been considered to quantify the RVE size, including having a more homogeneous force path network, having a smother stress-strain diagram, having a repetitive shear behavior, and having a higher chance of capturing the strain localization. Below, They will be explained in detail.

3.1.1. First criterion: Having a more homogeneous force chain network

All the particles will not participate equally in the deformation of the granular materials. However, when the forces between the particles are more symmetrical, the mechanical behavior of the material will be closer to the bulk state. Figure 6 shows the force chain

Table 2. The average of inter-particle forces and their standard deviation for the different size RVEs.

Number of the particles in the RVE	Average force (N)	Standard deviation (N)
150	13.72	10.68
300	12.65	9.94
500	12.84	10.55
1000	12.76	9.69
2000	12.71	10.13
3000	12.49	9.39
4000	14.53	9.87

Preprints (www.preprints.org) | NOT PEER-REVIEWED | Posted: 15 March 2021 doi:10.20944/preprints202103.0393.v1

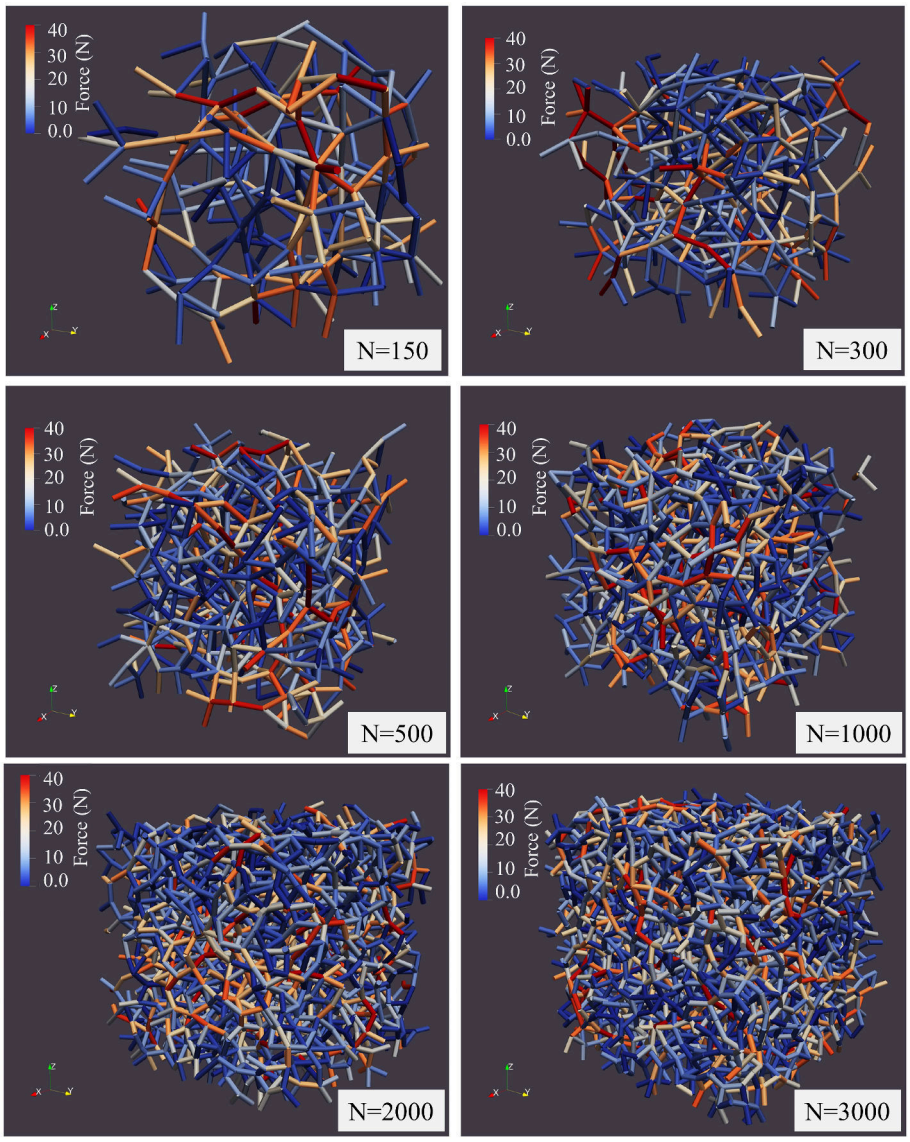

Figure 6. Force chain network for the RVE with the periodic boundary conditions.

network of RVEs with a different number of particles in which the RVEs are under confining pressure (P_0 = 100 kPa) and have periodic boundary conditions. To have an accurate explanation for Figure 6, the average of inter-particle forces and the standard deviation of the inter-particle forces are represented in Table 2. It is observed that the average of the inter-particle forces and their standard deviation are almost the same for all the RVEs. In addition, the results show that increasing the number of particles does not lead to an increase in the inter-particle forces. This can be due to the fact that the stress on the RVEs is the same. Hence, as the number of particles increases, both the boundary areas and the number of particles that apply force to the boundaries increase in order to keep the stresses felt at the boundaries constant. Therefore, this criterion does not lead us to a specific conclusion for selecting the appropriate number of particles in the RVE.

3.1.2. Second and third criteria: Smooth the stress-strain curve and repetitive behavior

For quantifying the smoothness and repetitive behavior, the shear response of the RVEs with a different number of particles are simulated and for each RVE this simulation is repeated five times, and then their average is calculated. Figure 7 shows the average shear behavior of the RVEs with different number of particles, and the error bars represent the standard deviation from the average behavior. Because the bulk behavior of the RVEs is

Preprints (www.preprints.org) | NOT PEER-REVIEWED | Posted: 15 March 2021 doi:10.20944/preprints202103.0393.v1

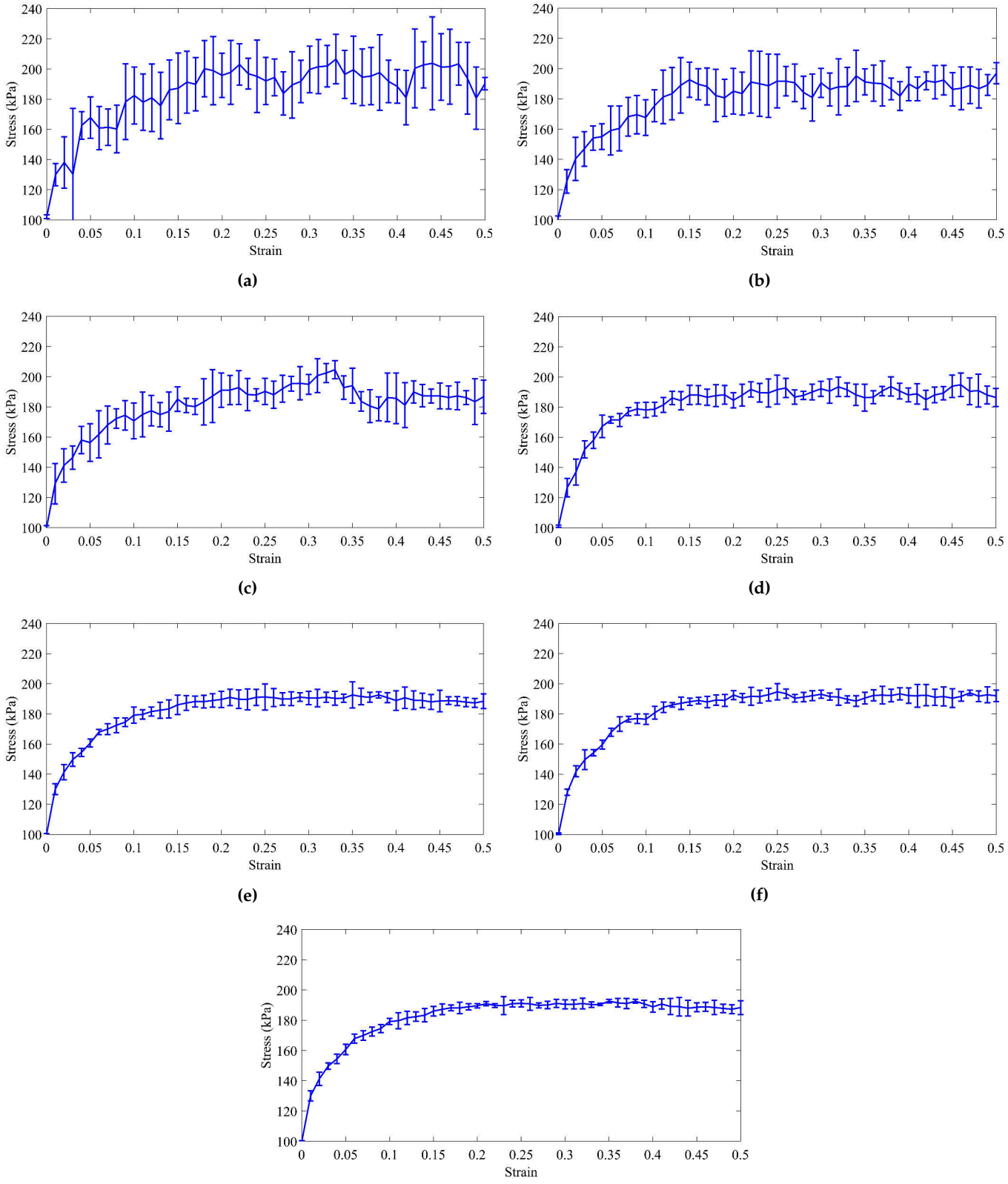

Figure 7. The average of shear behavior of the RVEs with (a) 150, (b) 300, (c) 500, (d) 1000, (e) 2000, (f) 3000, and (g) 4000 particles and periodic boundary conditions. The error bars indicate the standard deviation for five times of simulation for each RVE.

Preprints (www.preprints.org) | NOT PEER-REVIEWED | Posted: 15 March 2021 doi:10.20944/preprints202103.0393.v1

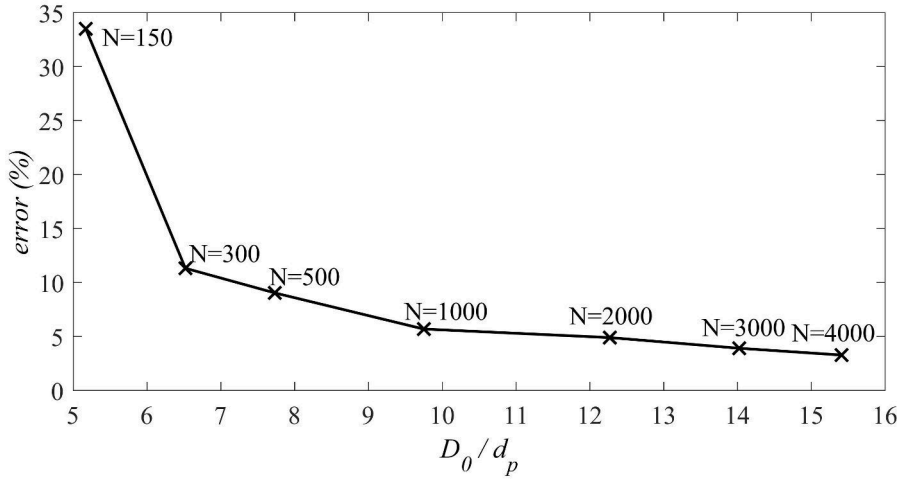

Figure 8. The maximum error of the stress-strain fluctuation versus D_0/d_p for the different RVEs with the different number of particles.

desired, the periodic boundary conditions are employed. The results show that increasing the number of particles leads to a reduction in the standard deviations and makes the average stress-strain behavior of the RVEs smoother. This is because as the number of particles increases, so does the number of particles taking part in the deformation. Also, since the deformation of the granular material is associated with buckling of the force chains and rearrangement of the particles, there are more particles to replace in the new force chains so that they can withstand the external loads. As a result, less stress the fluctuations are felt at the boundaries. Therefor, the stress-strain curve will be smoother.

To quantitative this phenomenon, D_0/d_p is considered in which D_0 is the size of the RVE at the beginning of the compaction process and d_p is the diameter of the particles. Based on [103], for the RVEs with higher D_0/d_p, the fluctuations of the stress-strain diagram are reduced. We define another parameter in which the ratio of the maximum of the standard deviation to its average stress is considered as the error parameter. The error parameter is as follows:

$$error = \frac{Max(\delta\sigma_i)}{\sigma_i} \times 100\,, \tag{18}$$

where $Max(\delta\sigma_i)$ is the maximum of the standard deviation and the σ_i is the average stress belongs to the maximum standard deviation. In addition, Oda and Kazama [32] by using photoelastic pictures taken from a biaxial test on a two-dimensional assembly of oval rods indicated that the thickness of localized bands is at least 7 times of the mean particle size. Therefore, the RVEs with 150 and 300 particles in which D_0/d_p is less than 7 will be refused for this criterion. Moreover, according to Evesque and Adjemian [103], if the number of particles increases, the error will be decreased. In figure 8, the error parameter is plotted in terms of the parameter D_0/d_p for the RVEs with different number of particle. For the RVEs with 2000, 3000, and 4000 particles, the error is 4.9%, 3.9%, and 3.28 %, respectively. In addition, the parameter D_0/d_p for the RVEs with 2000, 3000, and 4000 particles is 12.27, 14.023, 15.41, respectively. Therefore, these three RVEs can be considered as candidates. It is worth mentioning that to achieve an error of less than 1%, an RVE with at least 10^7 particles must be used [103].

3.1.3. Forth criterion: Higher chance of capturing the strain localization

According to Stroeven et al. [102], if the size of the RVE increases, the resolution for capturing the strain localization inside the RVE increases. In other words, by increasing the number of particles, the localized zone will be more distinguishable. To examine this issue, the RVEs with the mono-size particles and the solid boundary conditions with the different number of particles are considered. The initial position of particles inside the

Preprints (www.preprints.org) | NOT PEER-REVIEWED | Posted: 15 March 2021 doi:10.20944/preprints202103.0393.v1

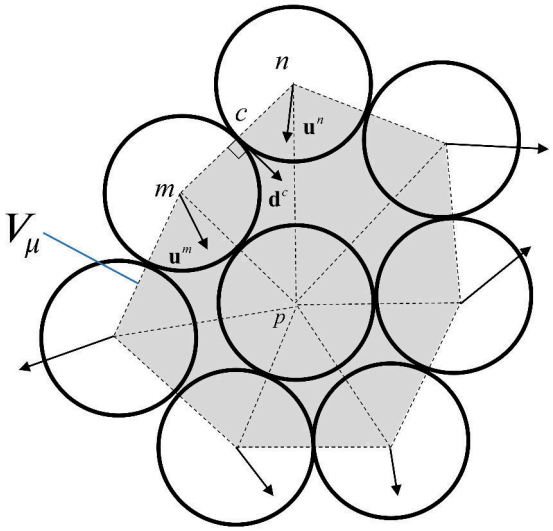

Figure 9. the particle-centered domains for the definition of micro-strain.

RVEs is random. The particles are initially compressed by a confining pressure of 100 kPa. While the axial pressure is applied through the upper displacement-controlled boundary ($\dot{\epsilon_3} = 0.05\ \mathrm{s}^{-1}$), the micro-strain is calculated for each particle. The micro-strain tensor for a particle is defined as a function of the displacements of the particles adjacent to it in the regular triangulation, which forms the polyhedral domain V_μ (Figure 9) [104,105]. The definition is based on the equivalent continuum formed by the space cells of the system. The space cells are triangles in 2D and tetrahedral in 3D, formed by the centers of neighboring (but not necessarily contacting) particles (see Figure 9). The boundary of this equivalent continuum goes through the center of the surrounded particles. The average displacement gradient in the equivalent continuum, which contains the polyhedral domain V_μ, is as follows:

$$\langle \nabla \mathbf{u} \rangle_\mu = \frac{1}{V_\mu} \iiint_{V_\mu} \frac{\partial(\mathbf{u})}{\partial \mathbf{x}}\, dV_\mu = \frac{1}{V_\mu} \iint_{S_\mu} \mathbf{u} \cdot \mathbf{n}\, dS_\mu\ , \tag{19}$$

where, V_μ and S_μ are the volume or the surface area of the cell, $d\mathbf{u}$ is the translation vector of the boundary point, and n is the outwards unit normal vector of the boundary of the cell at the same point. In addition, the amount of $d\mathbf{u}$ for the point c is equal to the difference between m and n nodes translation. Therefore, by applying the $\Delta\mathbf{u}^c = \mathbf{u}^n - \mathbf{u}^m$ and using $\mathbf{d}^c$, the complementary area vector belonging to the c the pair of grains (see [105,106] for more detail), the average displacement gradient for the particle p will be:

$$\langle \nabla \mathbf{u} \rangle_\mu = \frac{1}{V_\mu} \sum_c \Delta\mathbf{u}^c \mathbf{d}^c, \tag{20}$$

and the micro-strain is the symmetric part of Equation (20) and is as follows:

$$\langle \epsilon_{ij} \rangle_\mu = \frac{1}{2V_\mu} \sum_c \left(\Delta u_i{}^c d_j{}^c + \Delta u_j{}^c d_i{}^c\right). \tag{21}$$

The micro-strains are visualized for the different RVEs in Figure 10 and it roughly shows that localized areas are more recognizable as the number of particles increases. Hence, as shown in Figure 10, it is easier to detect the localized areas in the RVEs with 3000 and 4000 particles than in the RVEs with 1000 and 2000 particles. However, this judgment is based on the visualization (color difference in Figure 10) and mathematically it could not

Preprints (www.preprints.org) | NOT PEER-REVIEWED | Posted: 15 March 2021 doi:10.20944/preprints202103.0393.v1

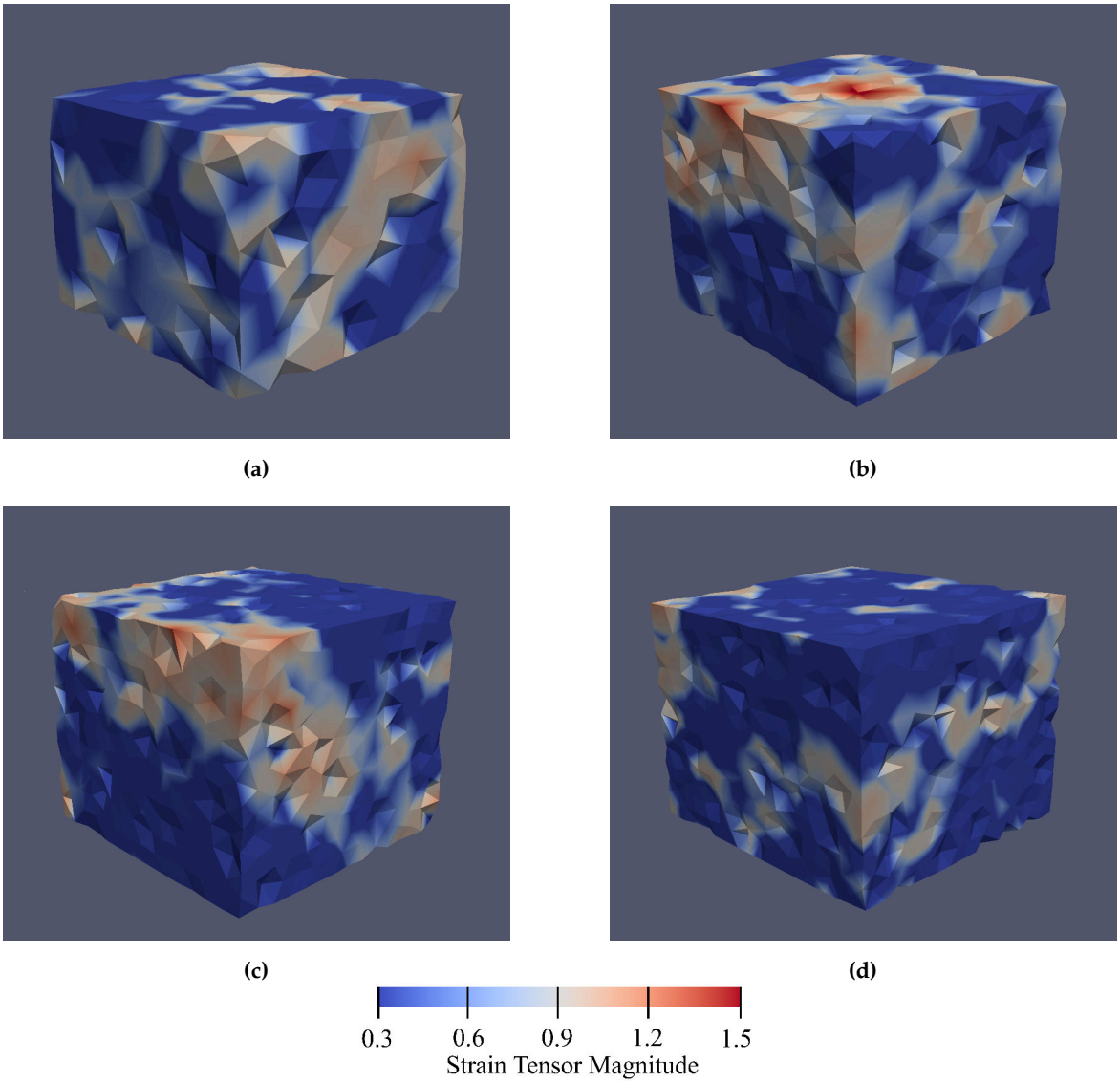

Figure 10. The magnitude of the micro-strain insideThe RVEs with (a) 1000, (b) 2000, (c) 3000, and (d) 4000 particles.

be cited. Hence, we need a rational criterion to select the RVE with the most probable of the strain localization formation.

As explained in Section 2.1, the granular material failure is a transition state (a bifurcation) between a quasi-static regime and a dynamic one; consequently, the changing procedure of the kinetic energy could be a reliable indicator of the granular material failure [92,93]. Therefore, by pursuing of the kinetic energy of a granular system, its failure can be recognized. In addition, As Oda and Kazama [32] explained, the particles which are located in the localized zone have the rotation one order of the magnitude more than the rotation of the particles outside of the localized zone. Hence, the onset of failure will be accompanied by a jump in the kinetic energy of the granular system [92]. The kinetic energy of a granular system is:

$$\mathcal{K}(t) = \sum_{i=1}^{\mathrm{N}} \left[\frac{1}{2} m^p (v^p)^2 + \frac{1}{2} \omega^p \left(I^p \omega^{pT} \right) \right], \tag{22}$$

where m^p is the mass of the particle p, v^p is the linear velocity of the particle p, I^p is the inertia tensor transformed to the global frame, and ω^p is the angular velocity of the particles p. The total number of the particles in each RVE is denoted by N. In view of the

Preprints (www.preprints.org) | NOT PEER-REVIEWED | Posted: 15 March 2021 doi:10.20944/preprints202103.0393.v1

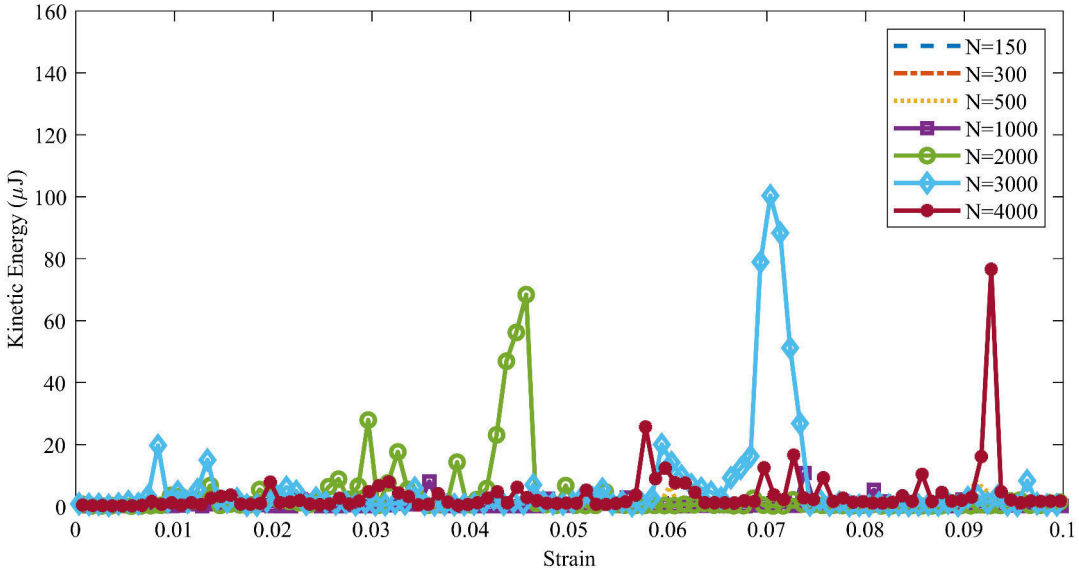

Figure 11. The evolution of the total kinetic energy of different RVEs during the compaction process.

fact that the compaction process carried out in the quasi static manner, the kinetic energy of all the RVEs will remain near to zero ($10^{-2}\mu$J) except when the failure occurs in them. It should be note that the discrete element method is a dynamic method (in each step, DEM solves Newton's second law of motion for each particle to find the new interactions and position of particles), hence the initial kinetic energy of the system is not exactly zero (the initial kinetic energy is in the order of $10^{-2}\mu$J). Therefore, the outburst of the kinetic energy is an indicator of the higher probability of the failure (localization) in the RVEs. Figure 11 shows the kinetic energy evaluation of the RVEs with different number of particles. For the RVEs with 2000, 3000, and 4000 particles, the kinetic energy diagram has a jump when the strain equal to 0.044, 0.07, and 0.093, respectively. The local maximums of Figure 11 reveal the bucking of the small force-chains in the RVEs [107]. Therefore, the RVEs with 2000, 3000, and 4000 particles can be treated as candidates.

All the criteria which are considered in this paper show that as the number of particles increases, the RVE behavior will be more reliable. On the other hand, increasing the number of particles dramatically affects the computational cost. Therefore, selecting the size of the RVE size is a trade-off between the computational cost and the reliability of the results. The computational cost for DEM simulation is a function of the number of particles, strain rate, the hydrostatic pressure, and the Central Processing Units (CPU) of the system used for the simulation. For example, the computational cost for the RVE with 1000 particles, confining pressure equal to 100 kPa, and the strain rate equal to 0.05 s^{-1} is approximately 10 hours. This time for the RVE with 4000 particles is nearly four days. Therefore, the computational cost is the most effective limiting factor for considering more particles. According to our criteria, the error and smoothness of the RVE with 3000 and 4000 particles are almost the same. Hence, to reduce the computational cost, the RVE with 3000 particles will be considered for further investigations.

4. Failure analysis

The confining pressure and the speed of compaction process have a significant effect on the final density of the carbon anodes. To investigate the effect of the confining pressure and the strain rate on the failure of the carbon anodes, numerical simulations were conducted on three three-dimensional specimens S_1, S_2, and S_3 which are compacted uniformly by confining pressure equal to 100 kPa, 250 kPa, and 100 kPa, respectively. All of the specimens are cubical in shape and contain 3000 spherical particles of radius 1.87 mm enclosed within six rigid frictionless walls. They were compressed from initially sparse arrangements of the particles to an isotopic state by moving the six rigid frictionless walls until the desired

Preprints (www.preprints.org) | NOT PEER-REVIEWED | Posted: 15 March 2021 doi:10.20944/preprints202103.0393.v1

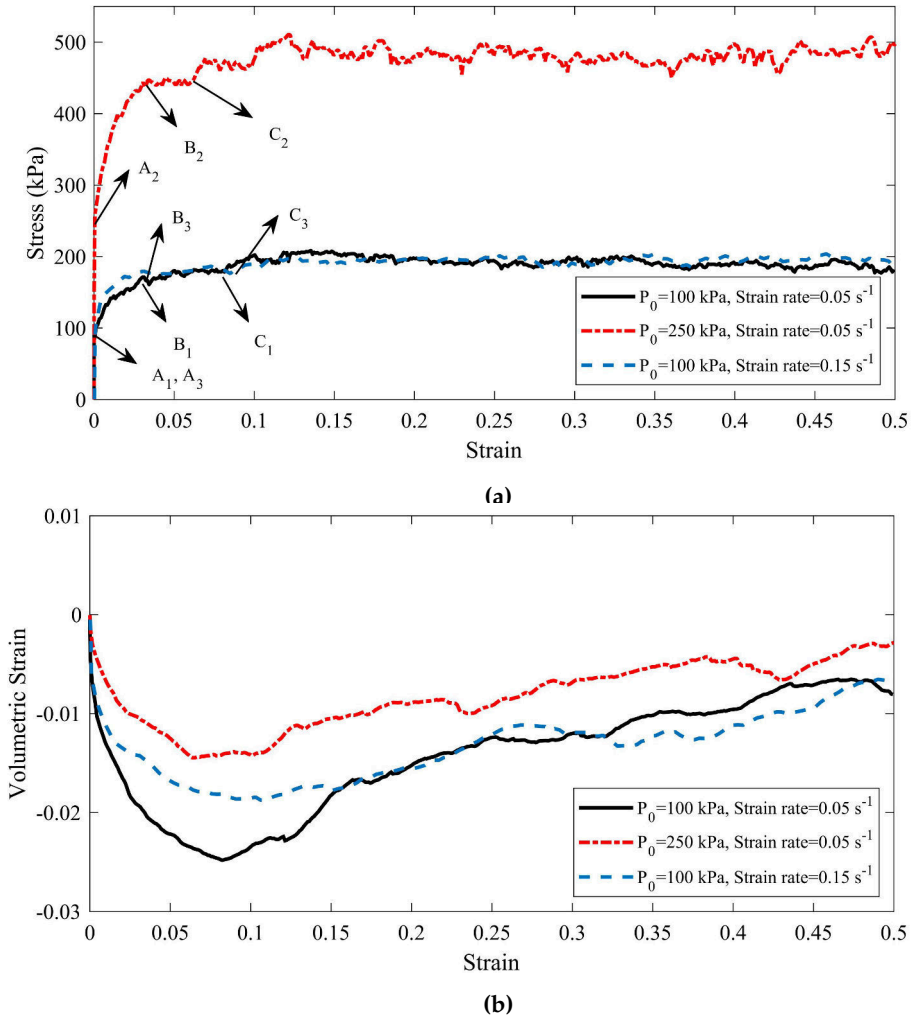

Figure 12. (a)The shear stress behavior and (b) the volumetric strain behavior of specimens S_1, S_2, and S_3.

confining pressures are reached. The desired confining pressures for specimens S_1 and S_3 are $\sigma_1 = \sigma_2 = \sigma_3 = 100$ kPa and for specimen S_2 is $\sigma_1 = \sigma_2 = \sigma_3 = 250$ kPa. They are then subjected to a drained conventional triaxial compression loading path. The stresses are kept constant and equal to confining pressures in the lateral directions. The specimens are loaded by applying constant strain rate in the axial direction. The axial strain rate for specimen S_1 and S_2 is $\dot{\epsilon}_3 = 0.05\ \mathrm{s}^{-1}$, for specimen S_3 is $\dot{\epsilon}_3 = 0.15\ \mathrm{s}^{-1}$. The initial porosity of both specimens S_1 and S_3 are the same and equal to $\phi = 0.466$. The initial porosity of the specimen S_2 is equal to $\phi = 0.463$. It should be noticed that porosity is defined as $\phi = \frac{V_T - V_s}{V_T}$ in which V_s is the volume of spheres and V_T is the total volume of specimen.

The evolution of both the axial stress σ_3 and the volumetric strain ϵ_v versus the axial strain ϵ_3 are shown in Figure 12 (a) and (b), respectively for all three specimens. For specimen S_1, the axial stress increases continuously (positive hardening regime) toward a limit plateau at which $\sigma_3 = 203$ kPa, and its volumetric strain increases when the strain reaches to 0.0825. By increasing the confining pressure for specimen S_2, the hardening regime augments and its axial stress increases until it reaches to the strain $\epsilon_3 = 0.122$. The maximum of the axial stress at this strain is $\sigma_3 = 511$ kPa. Its volumetric strain grows after axial strain reaches to $\epsilon_3 = 0.067$. The shear behavior of specimen S_3 is similar to specimen S_1, except that the hardening regime for specimen S_3 is shorter than specimen S_1 and it reach to its maximum level of stress when the axial strain is equal to 0.0365. Moreover, the reduction of volumetric strain for specimen S_3 is less than specimen S_1 and it attains its minimum value at the axial strain $\epsilon_3 = 0.92$. These analyzes are based on the behavior of the granular material at the boundaries. Although our information in the laboratory

Preprints (www.preprints.org) | NOT PEER-REVIEWED | Posted: 15 March 2021 doi:10.20944/preprints202103.0393.v1

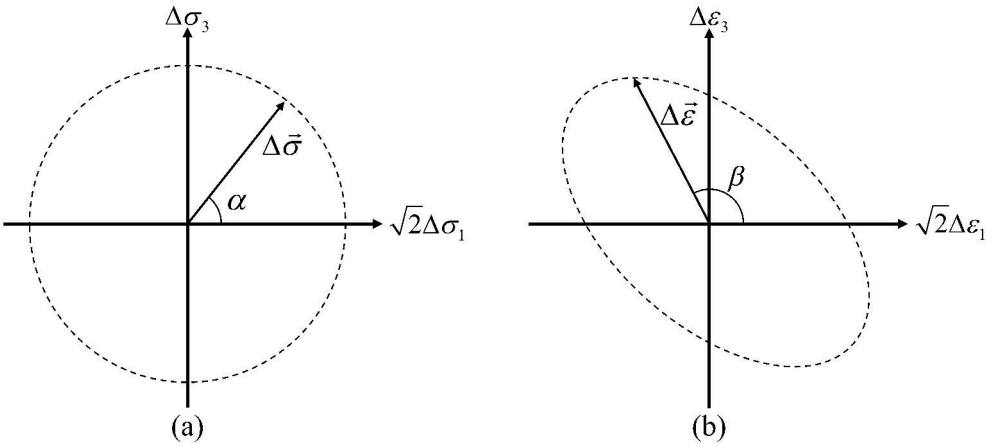

Figure 13. Definition of Rendulic planes; (a) stress probes and (b) strain responses.

experiments is also based on the information which are obtained from the boundaries, when the granular materials fails, the information at the boundaries does not properly delineate the behavior of the material. Therefore, second-order work analysis requires examining the behavior of the specimens at their critical points.

4.1. Second-order work from macroscopic variables

In Section 2, the two distinct formulations of the second-order work have been reviewed. [42] shown that the semi-Lagrangian and the Eulerian expressions of the second-order work are equivalent as long as the deformation is quasi static. In addition, the second-order work for a granular material can be calculated using by either macroscopic variable or inter-particle variables (microscopic variables) [39]. [42] shown that the macroscopic second-order work Equation (1) (the variables that are measured at the boundaries) and the microscopic expression (which takes into account the forces between the particles and the micro displacement gradient) are in a good agreement. Therefore, in this paper, the Eulerian expression of the second-order work with macroscopic variable will be used.

In order to compute the second order work from the macroscopic variables, three stress states defined by their deviatoric stress ratio $\eta = (3(\sigma_3 - \sigma_1)/(\sigma_1 + \sigma_2 + \sigma_3))$ are considered (represented by the points (A_1, B_1, C_1), (A_2, B_2, C_2), and (A_3, B_3, C_3) in Figure 12 (a) for specimens S_1, S_2, and S_3, respectively). These arbitrary stress states are chosen before the maximum stress condition (Mohr-Coulomb condition) is reached (see Table 3). In particular, A_1, A_2, and A_3 correspond to the isotropic state for each specimen. The strain states which are specified in Table 3 will constitute initial states on which stress probes (as first introduced by [108]) are performed. It should be noted that due to frictionless boundaries of specimens and the fact that lateral stresses are kept equal, the stress probe will be written as:

$$\Delta\vec{\sigma} = \| \Delta\vec{\sigma} \| (\cos(\alpha)\vec{e_1} + \cos(\alpha)\vec{e_2} + \sin(\alpha)\vec{e_3}) . \tag{23}$$

Table 3. Deviatoric stress ratio η and axial strain ϵ_3 corresponding to the critical points of specimens S_1, S_2, and S_3.

	Specimen S_1			Specimen S_2			Specimen S_3		
	A_1	B_1	C_1	A_2	B_2	C_2	A_3	B_3	C_3
ϵ_3	0	0.0413	0.0833	0	0.0365	0.067	0	0.04	0.092
η	0	0.69	0.74	0	0.62	0.76	0	0.65	0.75

Preprints (www.preprints.org) | NOT PEER-REVIEWED | Posted: 15 March 2021 doi:10.20944/preprints202103.0393.v1

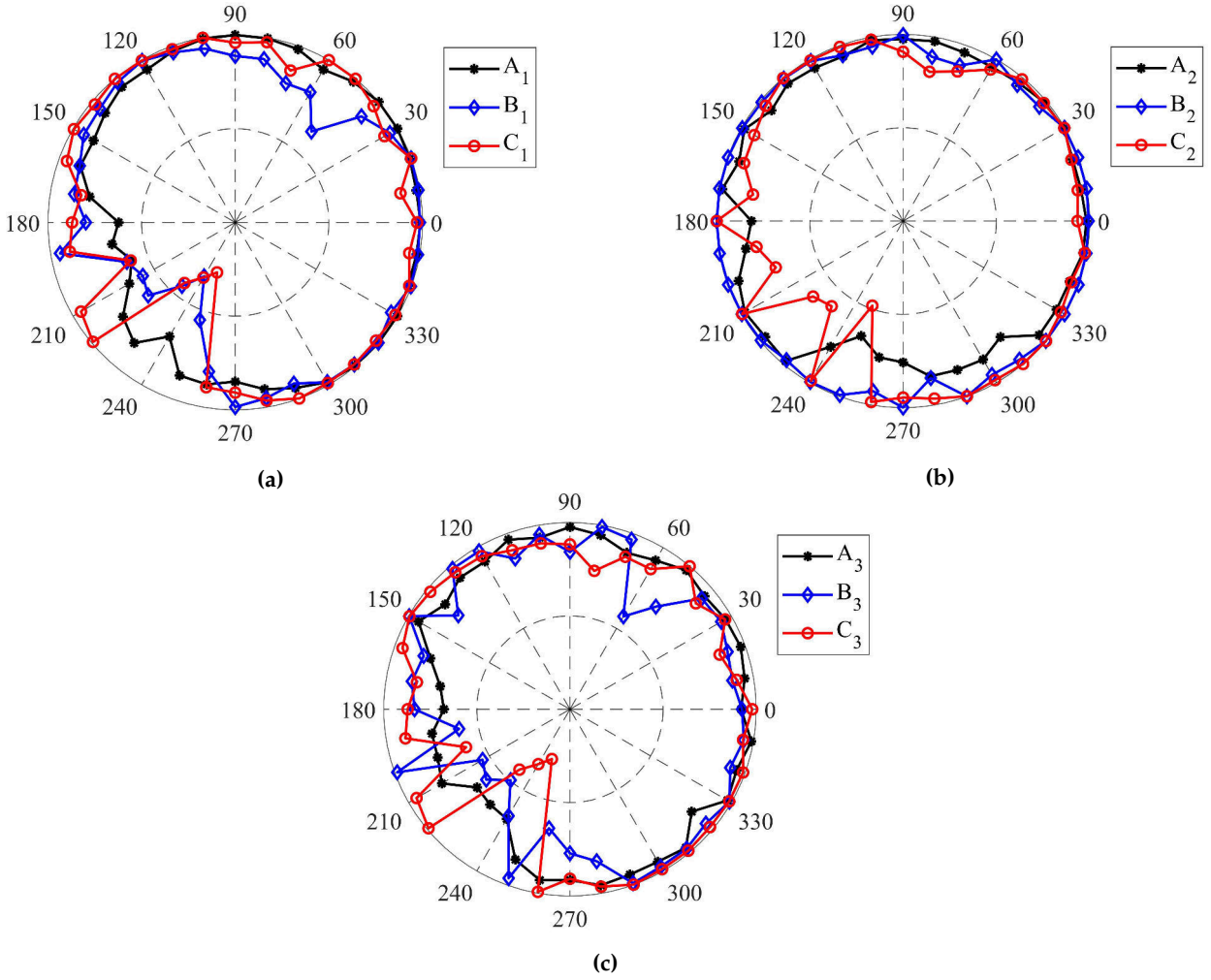

Figure 14. Circular diagrams of the normalized second-order work of (a) specimen S_1 (confining pressure $P_0 = 100$ kPa and strain rate $\dot{\epsilon_3} = 0.05\ s^{-1}$), (b) specimen S_2 (confining pressure $P_0 = 250$ kPa and strain rate $\dot{\epsilon_3} = 0.05\ s^{-1}$), and (c) specimen S_3 (confining pressure $P_0 = 100$ kPa and strain rate $\dot{\epsilon_3} = 0.15\ s^{-1}$) for different values of η.

By exposing this stress probe to the specimens, the strain response will be obtained directly from DEM as:

$$\Delta\vec{\epsilon} = (\parallel \Delta\vec{\epsilon_1} \parallel)\vec{e_1} + (\parallel \Delta\vec{\epsilon_2} \parallel)\vec{e_2} + (\parallel \Delta\vec{\epsilon_3} \parallel)\vec{e_3}\ . \tag{24}$$

As the stress probe and its strain response are equal in the lateral direction, the they could be represented on a two dimensional diagram (see Figure 13). Stress probes are performed from an initial stress-strain state by imposing a loading vector $\Delta\vec{\sigma}$ defined in the Rendulic plane of stress increments $(\sqrt{2}\Delta\sigma_1, \Delta\sigma_3)$. The norm of $\Delta\vec{\sigma}$ assumed to be 10 kPa. The angle α between the $\sqrt{2}\Delta\sigma_1$ and $\Delta\vec{\sigma}$ is increased from 0° to 360° by increments of 10° to check each stress direction. The maximum axial strain rate for applying the stress probe for specimens S_1 and S_2 is equal to $0.05\ s^{-1}$, and for the specimen S_3 is equal to $0.15\ s^{-1}$. The corresponding response vectors $\Delta\vec{\epsilon}$, defined in the Rendulic plane of the strain increments $(\sqrt{2}\Delta\epsilon_1, \Delta\epsilon_3)$ are computed. Once the strain response $\Delta\vec{\epsilon}$ is computed for each stress probe, by using Eulerian expression of Equation (1) the macroscopic normalized second-order work is computed as:

$$d^2\bar{W} = \frac{\Delta\vec{\sigma}.\Delta\vec{\epsilon}}{\parallel \Delta\vec{\sigma} \parallel \parallel \Delta\vec{\epsilon} \parallel}\ , \tag{25}$$

for all investigated stress directions and considered strain states. It is worth mentioning that the value of normalized second-order work is in the range of $[-1, 1]$. Figure 14 represents the value of the normalized second-order work for the specimens S_1, S_2, and S_3 at their

Preprints (www.preprints.org) | NOT PEER-REVIEWED | Posted: 15 March 2021 doi:10.20944/preprints202103.0393.v1

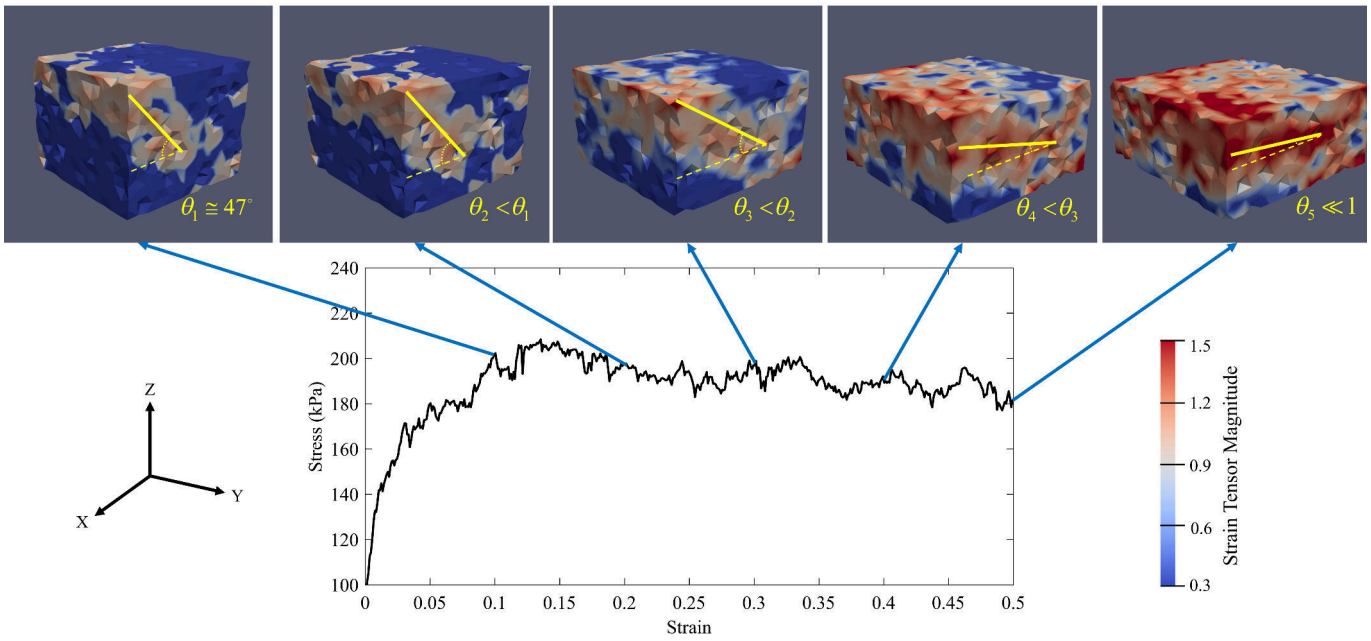

Figure 15. The micro-strain contour evolution during compaction process of specimen S_1 ($P_0 = 100$ kPa and $\dot{\epsilon_3} = 0.05 s^{-1}$).

critical stress state. The dashed circles in Figure 14 demonstrate the zero value for the second-order work. Therefore, when $d^2\bar{W}$ is negative the plot is inside the dashed circles, whereas plot is outside the dashed circles for positive values of $d^2\bar{W}$.

All the specimens have a positive second-order work in the isotropic stress state (points A_1, A_2, and A_3). In the other words, all the specimens are in the stable stress state at the begging of the compaction process. For the specimen S_1, the cone of the unstable stress directions (inside the dashed circle zone in Figure 14 (a)) are found for $\sigma_3 = 173.5$ kPa when its correspond α is in the range of $[225^\circ, 248^\circ]$. In addition, the stress states of point C_1, in which the tangent of the volumetric strain diagram (Figure 12 (b)) is zero, are unstable when α in the range of $[227^\circ, 254^\circ]$. By increasing the confining pressure for specimen S_2 to $P_0 = 250$ kPa, all the stress states associated with point B_2 are stable. Moreover, the unstable stress is discovered for the $\sigma_3 = 445$ kPa when its corresponding α is in the range of $[249^\circ, 251^\circ]$. The results indicates that by enhancing the confining pressure, the stable zone for the compaction process increases, and the specimen could be tolerated more stress without any failure inside. In a similar way, by increasing the strain rate to $\dot{\epsilon_3} = 0.15\ s^{-1}$, the cone of the unstable stress directions are found when the axial stress is equal to 174.1 kPa (Figure 14 (c)). The unstable corresponding α for this stress state is in the range of $[229^\circ, 231^\circ]$. By comparison the range of the unstable α for the points B_1 and B_3 reveals that the unstable zone diminishes when the strain rate enhances. However, by analyzing the response of the stress state at the point C_3, the unstable stress directions are detected when the range of α is $[226^\circ, 253^\circ]$, which is almost similar to the range of the unstable α for the point C_1 of the specimen S_1. As we discussed in Section 2, the second-order work criterion does not specify the instability mode of specimens. Therefore, the micro-strain contours are plotted during the compaction process to identify which type of failure modes (localization or diffusing failure) is happened inside the specimens.

4.2. Failure mode along the drained compression path

Both modes of the failure, either the localized within the granular assembly forming then a system with failing bands and unloading zones; or diffuse within the whole granular assembly (as thoroughly investigated in [109]) are observable for the failures initiated from the generalized limit states. Thanks to using the micro-strain contours inside the specimens, the mode of failure could be recognizable. As discussed in the previous section, specimen S_1 fails when the axial stress and the axial strain are equal to 173.5 kPa and 0.0413,

Preprints (www.preprints.org) | NOT PEER-REVIEWED | Posted: 15 March 2021 doi:10.20944/preprints202103.0393.v1

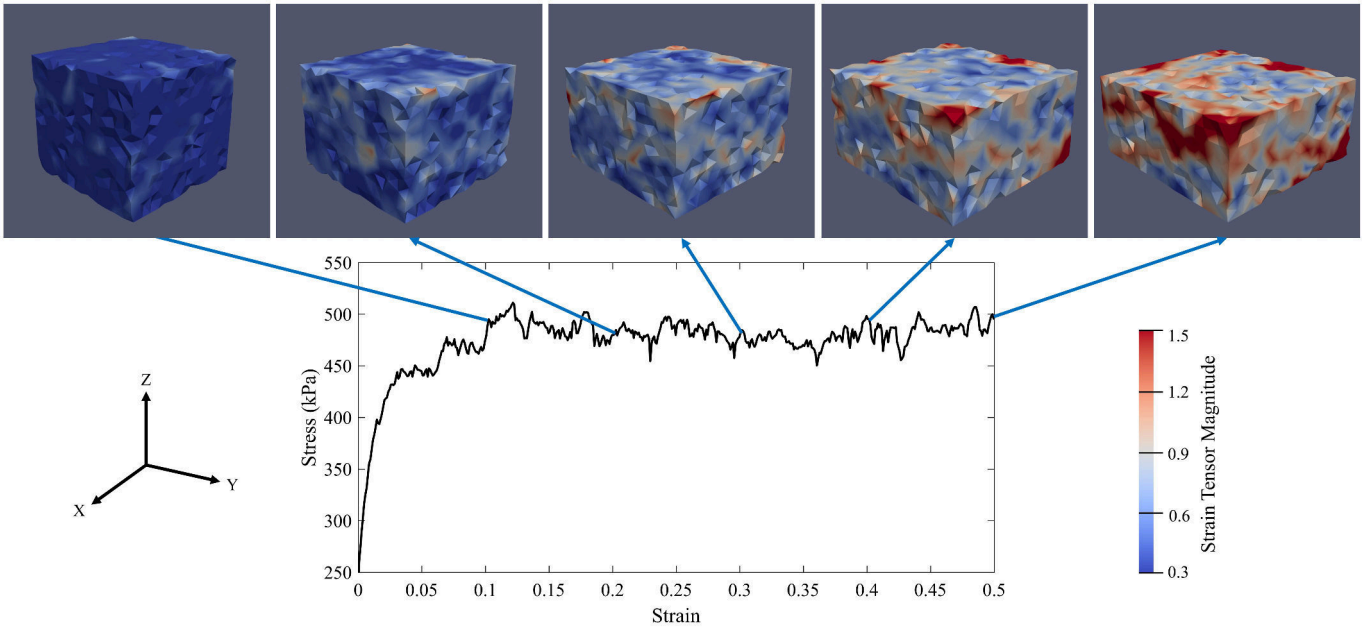

Figure 16. The micro-strain contour evolution during compaction process of specimen S_2 ($P_0 = 250$ kPa and $\dot{\epsilon_3} = 0.05s^{-1}$).

respectively. The localization area is distinguishable in Figure 15. This figure presents the evolution of the localized area from the shear band to the compaction band of specimen S_1. At the beginning of the compaction, the micro-strain inside the specimen is uniform. By increasing the compaction in the z-direction, the micro-strain localizes in the specimen. Because the initial angle between the localized band and the the maximum principal stress plane (here XY-plane) is not zero ($\theta_1 \cong 47^\circ$), there are shear stresses within the localized zone. It means that the localized zone is a shear band. By increasing the compaction, the angle decreases to a value very close to zero ($\theta_5 \simeq 0$). The zero angle means that there is no shear stress in the localized band. Hence, the localized band is a compaction band at the end of the compaction. In other words, the shear band becomes the compaction band. These results are consistent with the results of Das et al. [110]. Therefore, as discussed earlier, the compaction band creates a region that is prone to horizontal crack formation.

In Figure 16, the micro-strain contours are depicted for specimen S_2. As shown in Figure 14 (b), specimen S_2 fails when it reach to the axial stress 471 kPa and the axial strain 0.067. The micro-strain contours reveal that no specific localization pattern could be seen inside the sample. Therefore, it could be deduced that when confining pressure increases, the failure mode of the specimen intents to be a diffusing failure. It is worth to know that the dead-weight of the vibro-compactor in the anode production indicates the confining pressure. Consequently, enhancing the dead-weight of the vibro-compactor can be used as a proposed solution to prevent the strain localization in the carbon anodes.

On the other hand, according to Figure 14 (c), specimen S_3 fails when its axial stress and axial strain are equal to 189 kPa and 0.092, respectively. Figure 17 shows that the strain localization mode of failure is predominant in specimen S_3 and similar to the compaction process of specimen S_1, the localized band of specimen S_3 is a type of shear band at the beginning of the compaction process. The angle between the shear band and the maximum principal stress plane (here XY-plane) at the axial strain $\epsilon_3 = 0.1$ is equal to 42°. Although the shear band angle (θ_i) decreases as the axial strain increases, the shear band remains a shear band at the end of the compaction process ($\theta_5 \cong 18^\circ$). It means that increasing the axial strain rate will postpone the formation of the compaction bands. Therefore, the compaction process can be continued further until the shear band angle reaches close to zero (the shear band turns to a compaction band). Hence, by taking into account the fact that the vibro-compactor frequency in the anode production process represents the amount

Preprints (www.preprints.org) | NOT PEER-REVIEWED | Posted: 15 March 2021 doi:10.20944/preprints202103.0393.v1

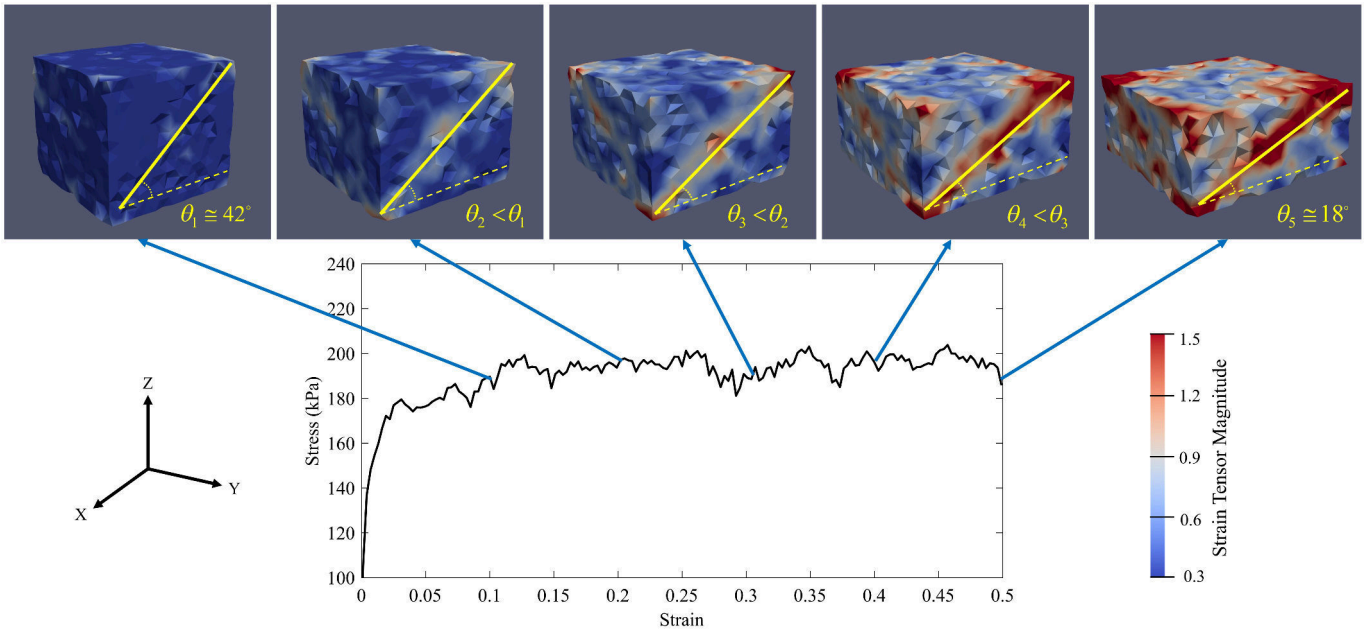

Figure 17. The micro-strain contour evolution during compaction process of specimen S_3 ($P_0 = 100$ kPa and $\dot{\epsilon_3} = 0.15 s^{-1}$).

of the axial strain rate, increasing the frequency can be a suggested solution to inhibit the formation of compaction bands in the anode production process.

5. Conclusions

This paper presents a theoretical aspect of the failure analysis in the granular material and a numerical investigation to find the failure in the mono-sized spherical coke aggregate under different compaction conditions. Some conclusions can be summarized as follows:

- It has been shown that the strain localization could happen in the carbon anodes during the compaction process and if this localized zone be a type of the compaction band, it could be responsible for the crack generation under the stub-holes in the carbon anodes. As the carbon anode paste behavior during the compaction process is too complex for considering, the dry mono-sized spherical coke aggregates have been examined.
- Considering failure as a bifurcation from a quasi-static regime to a dynamical one, a failure criterion was inferred, and the notion of the bifurcation domain was specified. The relationship between the kinetic energy of the granular materials and the internal and external second-order work has been evolved. It has been shown that when the failure occurred, the stresses which sense at the boundaries cannot reflect the real stress inside the material.
- Using the DEM simulation, the optimum number of particles which could represent the bulk material for the failure analysis is justified. Four criteria, including having a more uniform force path network, having a smother stress-strain diagram, repetitive behavior of the RVE, and a higher chance of the capturing the strain localization, have been exploited. It has been proved that the RVE with 3000 particles could represent the bulk material behavior in the failure analysis.
- The second-order criterion was used for finding the failure threshold in the specimens. The evolution of the shear band to the compaction band was investigated. Moreover, the effect of the confining pressure and the strain rate on the failure of the specimens have been studied. It revealed that by enhancing the confining pressure, the failure mode of the specimen would be of the diffusing type. However, by increasing the strain rate, the mode of the failure would be the localized type. In addition, the strain rate could postpone the formation of the compaction band, which can generate a susceptible area for the crack generation. The results highlighted that increasing the

Preprints (www.preprints.org) | NOT PEER-REVIEWED | Posted: 15 March 2021 doi:10.20944/preprints202103.0393.v1

confining pressure and the axial strain rate could be suggested solutions for preventing the localization or postponing the formation of the compaction bands in the carbon anode.

This article focuses on the study of the failure behavior of the dry mono-sized coke aggregates. However, the coke aggregates are very complex as they are composed of particles of different sizes, different shapes, different materials, etc. In the next step, the role of the size distribution and particle shape on the failure of the coke aggregates will be explored by using DEM simulation.

Appendix A

Let us consider, at a given time t, a homogeneous granular assembly of volume V in equilibrium under prescribed boundary conditions. Then, the rate of the deformation gradient tensor can be obtained as [97]:

$$\dot{\mathbf{F}} = \nabla \mathbf{v}\, \mathbf{F}. \tag{A1}$$

In the other hand, we can use a pull-back transportation to bring the differential from the spatial configuration to the material configuration as:

$$\nabla \mathbf{v} = \frac{\partial \mathbf{v}}{\partial \mathbf{X}} \frac{\partial \mathbf{X}}{\partial \mathbf{x}} = \frac{\partial \mathbf{v}}{\partial \mathbf{X}} \mathbf{F}^{-1}. \tag{A2}$$

By substituting Equation (A2) in (A1), it comes:

$$\dot{\mathbf{F}} = \left(\frac{\partial \mathbf{v}}{\partial \mathbf{X}} \mathbf{F}^{-1} \right) \mathbf{F} = \frac{\partial \mathbf{v}}{\partial \mathbf{X}}. \tag{A3}$$

Then, the mean value of the rate of the deformation gradient tensor ($\langle \dot{F}_{ij} \rangle$) by using Green formula is equal to:

$$\langle \dot{F}_{ij} \rangle = \frac{1}{V_0} \left(\iiint_{V_0} \frac{\partial v_i}{\partial X_j} dV_0 \right) = \frac{1}{V_0} \left(\iint_{S_0} v_i N_i dS_0 \right) = \frac{A_i \dot{u}_i}{V_0}. \tag{A4}$$

Appendix B

By using a similar process, we can calculate the second rate of the deformation gradient tensor by using a time derivative of Equation (A3):

$$\ddot{\mathbf{F}} = \frac{\partial}{\partial t} \left(\frac{\partial \mathbf{v}}{\partial \mathbf{X}} \right) \tag{A5}$$

Because $\mathbf{X}$ is independent of t, it can be written:

$$\ddot{\mathbf{F}} = \frac{\partial}{\partial \mathbf{X}} \left(\frac{\partial \mathbf{v}}{\partial t} \right). \tag{A6}$$

Then, by using Green formula, the mean value of the second rate of the deformation gradient tensor ($\langle \ddot{F}_{ij} \rangle$) is equal to:

$$\langle \ddot{F}_{ij} \rangle = \frac{1}{V_0} \left(\iiint_{V_0} \frac{\partial}{\partial X_j} \left(\frac{\partial v_i}{\partial t} \right) dV_0 \right) = \frac{1}{V_0} \left(\iint_{S_0} \left(\frac{\partial v_i}{\partial t} \right) \cdot N_j \, dS_0 \right) = \frac{A_i \ddot{u}_i}{V_0}. \tag{A7}$$

Author Contributions: Conceptualization, methodology, investigation, and writing—original draft preparation, A.S.C.; Writing-review and editing, R.M., D.P., J.T., S.M.T, and H.A.; supervision, H.A.; All authors have read and agreed to the published version of the manuscript

Preprints (www.preprints.org) | NOT PEER-REVIEWED | Posted: 15 March 2021 doi:10.20944/preprints202103.0393.v1

Funding: A part of the research presented in this article was financed by the Fonds de recherche du Québec – Nature et Technologies by the intermediary of the Aluminium Research Centre – REGAL.

Acknowledgments: The authors gratefully acknowledge the financial support provided by Alcoa Inc., the Natural Sciences and Engineering Research Council of Canada and Centre Québécois de Recherche et de Développement de l'Aluminium. We would like to express our very great appreciation to Dr. Donald Ziegler for his valuable and constructive suggestions during the planning and development of this research work.

Conflicts of Interest: The authors declare no conflict of interest.

References

1. Welch, B.J. Aluminum production paths in the new millennium. *JoM* **1999**, *51*, 24–28. https://doi.org/10.1007/s11837-999-0036-4.
2. Rhedey, P. A Review of factors affecting carbon anode consumption in the electrolytic production of aluminum. *Essent. Read. Light Met.* **2016**, pp. 611–622. https://doi.org/10.1007/978-3-319-48200-2_81.
3. Hulse, K.L. *Anode manufacture: raw materials, formulation and processing parameters*; R& D Carbon Limited, 2000.
4. Boubaker, M.B.; Picard, D.; Duchesne, C.; Tessier, J.; Alamdari, H.; Fafard, M. Non-destructive testing of baked anodes based on modal analysis and principal component analysis. In *Light Met.*; Springer, Cham, 2017; pp. 1289–1298. https://doi.org/10.1007/978-3-319-51541-0_154.
5. Dorcheh, K.A. Investigation of the materials and paste relationships to improve forming process and anode quality. PhD thesis, Université Laval, Québec, Canada, 2013. http://hdl.handle.net/20.500.11794/24666.
6. Majidi, B. Discrete element method simulation of packing and rheological properties of coke and coke/pitch mixtures. PhD thesis, Université Laval, Québec, Canada, 2018. http://hdl.handle.net/20.500.11794/30959.
7. Azari, K.; Alamdari, H.; Ammar, H.; Fafard, M.; Adams, A.; Ziegler, D. Influence of mixing parameters on the density and compaction behavior of carbon anodes used in aluminum production. Adv. Mat. Res. Trans. Tech. Publ., 2012, Vol. 409, pp. 17–22. https://doi.org/10.4028/www.scientific.net/AMR.409.17.
8. Amrani, S.; Kocaefe, D.; Kocaefe, Y.; Morais, B.; Blaney, G. Effect of heating rate on the crack formation during baking in carbon anodes used in aluminum industry. In *Light Met.*; Springer, Cham, 2014; pp. 1175–1180. https://doi.org/10.1007/978-3-319-48144-9_196.
9. Amrani, S.; Kocaefe, D.; Kocaefe, Y.; Bhattacharyay, D.; Bouazara, M.; Morais, B. Characterization of cracking mechanisms of carbon anodes used in aluminum industry by optical microscopy and tomography. *J. Mater. Eng. Perform.* **2016**, *25*, 4274–4282. https://doi.org/10.1007/s11665-016-2257-3.
10. Chamam, Y.; Kocaefe, D.; Kocaefe, Y.; Bhattacharyay, D.; Morais, B. Effect of heating rate during baking on the properties of carbon anodes used in aluminum industry. In *Light Met.*; Springer, Cham, 2016; pp. 947–951. https://doi.org/10.1007/978-3-319-48251-4_159.
11. Menard, Y. Prebaked anode cracking and forming–reasons and solutions. Proceedings of 35th International ICSOBA Conference, Hamburg, Germany, 2017, pp. 2–5.
12. Amrani, S.; Kocaefe, D.; Kocaefe, Y.S.; Bhattacharyay, D.; Bouazara, M.; Coulombe, P. Evolution of anode properties during baking. *Int. J. Innov. Sci. Eng. Technol.* **2017**, *4*, 301–309.
13. Meier, M.W. *Cracking behaviour of anodes*; R & D Carbon, 1996.
14. Schneider, J.; Coste, B. Thermomechanical modelling of thermal shock in anodes. *Light Met.* **1993**, pp. 621–628.
15. Chaouki, H.; Picard, D.; Ziegler, D.; Azari, K.; Alamdari, H.; Fafard, M. Viscoplastic modeling of the green anode paste compaction process. *J. Appl. Mech.* **2016**, *83*. https://doi.org/10.1115/1.4031857.
16. Anderson, T.L. *Fracture mechanics: fundamentals and applications*; CRC press, 2017. https://doi.org/10.1201/9781315370293.
17. Chaouki, H.; Thibodeau, S.; Fafard, M.; Ziegler, D.; Alamdari, H. Characterization of the Hot Anode Paste Compaction Process: A Computational and Experimental Study. *Materials* **2019**, *12*, 800. https://doi.org/10.3390/ma12050800.
18. Andrade, J.E.; Avila, C.; Hall, S.; Lenoir, N.; Viggiani, G. Multiscale modeling and characterization of granular matter: from grain kinematics to continuum mechanics. *J. Mech. Phys. Solids* **2011**, *59*, 237–250. https://doi.org/10.1016/j.jmps.2010.10.009.
19. Majidi, B.; Melo, J.; Fafard, M.; Ziegler, D.; Alamdari, H. Packing density of irregular shape particles: DEM simulations applied to anode-grade coke aggregates. *Adv. Powder Technol.* **2015**, *26*, 1256–1262. https://doi.org/10.1016/j.apt.2015.06.008.
20. Majidi, B.; Rouget, G.; Fafard, M.; Ziegler, D.; Alamdari, H. Discrete element method investigation of bulk density and electrical resistivity of calcined coke mixes. *Metals* **2017**, *7*, 154. https://doi.org/10.3390/met7050154.
21. Rouget, G.; Majidi, B.; Picard, D.; Gauvin, G.; Ziegler, D.; Mashreghi, J.; Alamdari, H. Electrical resistivity measurement of petroleum coke powder by means of four-probe method. *Metall. Mater. Trans. B* **2017**, *48*, 2543–2550. https://doi.org/10.1007/s11663-017-1022-9.
22. Daouadji, A.; Darve, F.; Al Gali, H.; Hicher, P.; Laouafa, F.; Lignon, S.; Nicot, F.; Nova, R.; Pinheiro, M.; Prunier, F.; Sibille, L.; Wan, R. Diffuse failure in geomaterials: Experiments, theory and modelling. *Int. J. Numer. Anal. Methods Geomech.* **2011**, *35*, 1731–1773. https://doi.org/10.1002/nag.975.
23. Nicot, F.; Sibille, L.; Darve, F. Failure in Granular Materials: Macro and Micro Views. In *Bifurcations, Instabilities and Degradations in Geomaterials*; Springer, 2011; pp. 1–12. https://doi.org/10.1007/978-3-642-18284-6_1.

Preprints (www.preprints.org) | NOT PEER-REVIEWED | Posted: 15 March 2021 doi:10.20944/preprints202103.0393.v1

24. Nicot, F.; Darve, F. Diffuse and localized failure modes: two competing mechanisms. *Int. J. Numer. Anal. Methods Geomech.* **2011**, *35*, 586–601. https://doi.org/10.1002/nag.912.
25. Sibille, L.; Hadda, N.; Nicot, F.; Tordesillas, A.; Darve, F. Granular plasticity, a contribution from discrete mechanics. *J. Mech. Phys. Solids* **2015**, *75*, 119–139. https://doi.org/10.1016/j.jmps.2014.09.010.
26. Hadda, N.; Sibille, L.; Nicot, F.; Wan, R.; Darve, F. Failure in granular media from an energy viewpoint. *Granul. Matter* **2016**, *18*, 50. https://doi.org/10.1007/s10035-016-0639-8.
27. Chu, J.; Leong, W.; Loke, W.; Wanatowski, D. Instability of loose sand under drained conditions. *J. Geotech. Geoenviron. Eng.* **2012**, *138*, 207–216. https://doi.org/10.1061/(ASCE)GT.1943-5606.0000574.
28. Simitses, G.; Hodges, D.H. *Fundamentals of structural stability*; Butterworth-Heinemann, 2006.
29. Tordesillas, A.; Muthuswamy, M. On the modeling of confined buckling of force chains. *J. Mech. Phys. Solids* **2009**, *57*, 706–727. https://doi.org/10.1016/j.jmps.2009.01.005.
30. Ziegler, H. *Principles of structural stability*; Vol. 35, Birkhäuser, 2013.
31. Wan, R.; Pinheiro, M.; Daouadji, A.; Jrad, M.; Darve, F. Diffuse instabilities with transition to localization in loose granular materials. *Int. J. Numer. Anal. Methods Geomech.* **2013**, *37*, 1292–1311. https://doi.org/10.1002/nag.2085.
32. Oda, M.; Kazama, H. Microstructure of shear bands and its relation to the mechanisms of dilatancy and failure of dense granular soils. *Geotechnique* **1998**, *48*, 465–481. https://doi.org/10.1680/geot.1998.48.4.465.
33. Darve, F.; Flavigny, E.; Meghachou, M. Constitutive modelling and instabilities of soil behaviour. *Comput. Geotech.* **1995**, *17*, 203–224. https://doi.org/10.1016/0266-352X(95)93869-K.
34. Liapounoff, A. Problème général de la stabilité du mouvement. Annales de la Faculté des sciences de Toulouse: Mathématiques, 1907, Vol. 9, pp. 203–474. https://doi.org/10.5802/afst.246.
35. Nova, R. Controllability of the incremental response of soil specimens subjected to arbitrary loading programmes. *J. Mech. behav. Mater.* **1994**, *5*, 193–202. https://doi.org/10.1515/JMBM.1994.5.2.193.
36. Nicot, F.; Darve, F.; Dat Vu Khoa, H. Bifurcation and second-order work in geomaterials. *Int. J. Numer. Anal. Methods Geomech.* **2007**, *31*, 1007–1032. https://doi.org/10.1002/nag.573.
37. Chambon, R. Some theoretical results about second-order work, uniqueness, existence and controllability independent of the constitutive equation. In *Hill J. M., Selvadurai A. (eds) Mathematics and Mechanics of Granular Materials*; Springer, Dordrecht, 2005; pp. 53–61. https://doi.org/10.1007/1-4020-4183-7_4.
38. Darve, F.; Laouafa, F. Instabilities in granular materials and application to landslides. *Mech. Cohesive-frict. Mater.* **2000**, *5*, 627–652.
39. Nicot, F.; Darve, F. A micro-mechanical investigation of bifurcation in granular materials. *Int. J. Solids Struct.* **2007**, *44*, 6630–6652. https://doi.org/10.1016/j.ijsolstr.2007.03.002.
40. Hill, R. A general theory of uniqueness and stability in elastic-plastic solids. *J. the Mech. Phys. Solids* **1958**, *6*, 236–249. https://doi.org/10.1016/0022-5096(58)90029-2.
41. Darve, F.; Servant, G.; Laouafa, F.; Khoa, H. Failure in geomaterials: continuous and discrete analyses. *Comput. Methods Appl. Mech. Eng.* **2004**, *193*, 3057–3085. https://doi.org/10.1016/j.cma.2003.11.011.
42. Darve, F.; Sibille, L.; Daouadji, A.; Nicot, F. Bifurcations in granular media: macro-and micro-mechanics approaches. *Comptes Rendus Mécanique* **2007**, *335*, 496–515. https://doi.org/10.1016/j.crme.2007.08.005.
43. Lade, P.V. Instability, shear banding, and failure in granular materials. *Int. J.Solids Struct.* **2002**, *39*, 3337–3357.
44. Rice, J.R.; Rudnicki, J. A note on some features of the theory of localization of deformation. *Int. J. Solids Struct.* **1980**, *16*, 597–605. https://doi.org/10.1016/0020-7683(80)90019-0.
45. Aydin, A.; Borja, R.I.; Eichhubl, P. Geological and mathematical framework for failure modes in granular rock. *J. Struct. Geol.* **2006**, *28*, 83–98. https://doi.org/10.1016/j.jsg.2005.07.008.
46. Rudnicki, J.W.; Rice, J. Conditions for the localization of deformation in pressure-sensitive dilatant materials. *J. Mech. Phys. Solids* **1975**, *23*, 371–394. https://doi.org/10.1016/0022-5096(75)90001-0.
47. Borja, R.I. Bifurcation of elastoplastic solids to shear band mode at finite strain. *Comput. Methods Appl. Mech. Eng.* **2002**, *191*, 5287–5314. https://doi.org/10.1016/S0045-7825(02)00459-0.
48. Borja, R.I.; Aydin, A. Computational modeling of deformation bands in granular media. I. Geological and mathematical framework. *Comput. Methods Appl. Mech. Eng.* **2004**, *193*, 2667–2698. https://doi.org/10.1016/j.cma.2003.09.019.
49. Calvetti, F.; Combe, G.; Lanier, J. Experimental micromechanical analysis of a 2D granular material: relation between structure evolution and loading path. *Mech. Cohes. frict. Mater.* **1997**, *2*, 121–163.
50. Bésuelle, P.; Desrues, J.; Raynaud, S. Experimental characterisation of the localisation phenomenon inside a Vosges sandstone in a triaxial cell. *Int. J. Rock Mech. Min. Sci.* **2000**, *37*, 1223–1237. https://doi.org/10.1016/S1365-1609(00)00057-5.
51. Desrues, J.; Viggiani, G. Strain localization in sand: an overview of the experimental results obtained in Grenoble using stereophotogrammetry. *Int. J. Numer. Anal. Methods Geomech.* **2004**, *28*, 279–321. https://doi.org/10.1002/nag.338.
52. Zhuang, L.; Nakata, Y.; Kim, U.G.; Kim, D. Influence of relative density, particle shape, and stress path on the plane strain compression behavior of granular materials. *Acta Geotech.* **2014**, *9*, 241–255. https://doi.org/10.1007/s11440-013-0253-4.
53. Wu, K.; Pizette, P.; Becquart, F.; Remond, S.; Abriak, N.; Xu, W.; Liu, S. Experimental and numerical study of cylindrical triaxial test on mono-sized glass beads under quasi-static loading condition. *Adv. Powder Technol.* **2017**, *28*, 155–166. https://doi.org/10.1016/j.apt.2016.09.006.

Preprints (www.preprints.org) | NOT PEER-REVIEWED | Posted: 15 March 2021 doi:10.20944/preprints202103.0393.v1

54. Alikarami, R.; Andò, E.; Gkiousas-Kapnisis, M.; Torabi, A.; Viggiani, G. Strain localisation and grain breakage in sand under shearing at high mean stress: insights from in situ X-ray tomography. *Acta Geotech.* **2015**, *10*, 15–30. https://doi.org/10.1144/SP289.4.
55. Borja, R.I. Computational modeling of deformation bands in granular media. II. Numerical simulations. *Comput. Methods Appl. Mech. Eng.* **2004**, *193*, 2699–2718. https://doi.org/10.1016/j.cma.2003.09.018.
56. Andrade, J.E.; Borja, R.I. Capturing strain localization in dense sands with random density. *Int. J. Numer. Methods Eng.* **2006**, *67*, 1531–1564. https://doi.org/10.1002/nme.1673.
57. Wang, B.; Chen, Y.; Wong, T.f. A discrete element model for the development of compaction localization in granular rock. *J. Geophys. Res. Solid Earth* **2008**, *113*. https://doi.org/10.1029/2006JB004501.
58. Guo, N.; Zhao, J. 3D multiscale modeling of strain localization in granular media. *Comput. Geotech.* **2016**, *80*, 360–372. https://doi.org/10.1016/j.compgeo.2016.01.020.
59. Liang, W.; Zhao, J. Multiscale modeling of large deformation in geomechanics. *Int. J. Numer. Anal. Methods Geomech.* **2019**, *43*, 1080–1114. https://doi.org/10.1002/nag.2921.
60. Alshibli, K.A.; Alsaleh, M.I.; Voyiadjis, G.Z. Modelling strain localization in granular materials using micropolar theory: Numerical implementation and verification. *Int. J Numer. Anal. Methods Geomech.* **2006**, *30*, 1525–1544. https://doi.org/10.1002/nag.534.
61. De Borst, R. Simulation of strain localization: a reappraisal of the Cosserat continuum. *Eng. Comput.* **1991**. https://doi.org/10.1108/eb023842.
62. Tang, H.; Dong, Y.; Wang, T.; Dong, Y. Simulation of strain localization with discrete element-Cosserat continuum finite element two scale method for granular materials. *J. Mech. Phys. Solids* **2019**, *122*, 450–471. https://doi.org/10.1016/j.jmps.2018.09.029.
63. Scholtès, L.; Donzé, F.V. A DEM model for soft and hard rocks: role of grain interlocking on strength. *J. Mech. Phys. Solids* **2013**, *61*, 352–369. https://doi.org/10.1016/j.jmps.2012.10.005.
64. Liu, Y.; Sun, W.; Yuan, Z.; Fish, J. A nonlocal multiscale discrete-continuum model for predicting mechanical behavior of granular materials. *Int. J. Numer. Methods Eng.* **2016**, *106*, 129–160. https://doi.org/10.1002/nme.5139.
65. Wu, H.; Zhao, J.; Liang, W. Pattern transitions of localized deformation in high-porosity sandstones: Insights from multiscale analysis. *Comput. Geotech.* **2020**, *126*, 103733. https://doi.org/10.1016/j.compgeo.2020.103733.
66. Khoa, H.D.V.; Georgopoulos, I.O.; Darve, F.; Laouafa, F. Diffuse failure in geomaterials: Experiments and modelling. *Comput. Geotech.* **2006**, *33*, 1–14. https://doi.org/10.1016/j.compgeo.2006.01.002.
67. Lade, P.V. Static instability and liquefaction of loose fine sandy slopes. *J. Geotech. Eng.* **1992**, *118*, 51–71. https://doi.org/10.1061/(asce)0733-9410(1992)118:1(51).
68. Chu, J.; Leroueil, S.; Leong, W. Unstable behaviour of sand and its implication for slope instability. *Can. Geotech. J.* **2003**, *40*, 873–885. https://doi.org/10.1139/t03-039.
69. Borja, R.I. Conditions for instabilities in collapsible solids including volume implosion and compaction banding. *Acta Geotech.* **2006**, *1*, 107–122. https://doi.org/10.1007/s11440-006-0012-x.
70. Sun, W. A unified method to predict diffuse and localized instabilities in sands. *Geomech. Geoeng.* **2013**, *8*, 65–75. https://doi.org/10.1080/17486025.2012.695403.
71. Borja, R.I. Localized and diffuse bifurcations in porous rocks undergoing shear localization and cataclastic flow. In: Oñate E., Owen R. (eds) Computational Plasticity, Comput. Methods Appl. Sci. Springer, Dordrecht, 2007, Vol. 7, pp. 37–53. https://doi.org/10.1007/978-1-4020-6577-4_3.
72. Borja, R.I. Condition for liquefaction instability in fluid-saturated granular soils. *Acta Geotech.* **2006**, *1*, 211. https://doi.org/10.1007/s11440-006-0017-5.
73. Andrade, J.E. A predictive framework for liquefaction instability. *Géotechnique* **2009**, *59*, 673–682. https://doi.org/10.1680/geot.7.00087.
74. Sibille, L.; Donzé, F.V.; Nicot, F.; Chareyre, B.; Darve, F. From bifurcation to failure in a granular material: a DEM analysis. *Acta Geotech.* **2008**, *3*, 15. https://doi.org/10.1007/s11440-007-0035-y.
75. Aydin, A.; Johnson, A.M. Analysis of faulting in porous sandstones. *J. Struct. Geol.* **1983**, *5*, 19–31. https://doi.org/10.1016/0191-8141(83)90004-4.
76. Aydin, A. Small faults formed as deformation bands in sandstone. In *Rock Friction and Earthquake Prediction*; Springer, 1978; pp. 913–930. https://doi.org/10.1007/978-3-0348-7182-2_22.
77. Davatzes, N.C.; Aydin, A.; Eichhubl, P. Overprinting faulting mechanisms during the development of multiple fault sets in sandstone, Chimney Rock fault array, Utah, USA. *Tectonophysics* **2003**, *363*, 1–18. https://doi.org/10.1016/S0040-1951(02)00647-9.
78. Antonellini, M.A.; Aydin, A.; Pollard, D.D. Microstructure of deformation bands in porous sandstones at Arches National Park, Utah. *J. Struct. Geol.* **1994**, *16*, 941–959. https://doi.org/10.1016/0191-8141(94)90077-9.
79. Sternlof, K.R.; Karimi-Fard, M.; Pollard, D.; Durlofsky, L. Flow and transport effects of compaction bands in sandstone at scales relevant to aquifer and reservoir management. *Water Resour. Res.* **2006**, *42*. https://doi.org/10.1029/2005WR004664.
80. Mollema, P.; Antonellini, M. Compaction bands: a structural analog for anti-mode I cracks in aeolian sandstone. *Tectonophysics* **1996**, *267*, 209–228. https://doi.org/10.1016/S0040-1951(96)00098-4.
81. Sternlof, K.R.; Rudnicki, J.W.; Pollard, D.D. Anticrack inclusion model for compaction bands in sandstone. *J. Geophys. Res. B* **2005**, *110*. https://doi.org/10.1029/2005JB003764.

Preprints (www.preprints.org) | NOT PEER-REVIEWED | Posted: 15 March 2021 doi:10.20944/preprints202103.0393.v1

82. Holcomb, D.; Rudnicki, J.W.; Issen, K.A.; Sternlof, K. Compaction localization in the Earth and the laboratory: state of the research and research directions. *Acta Geotech.* **2007**, *2*, 1–15. https://doi.org/10.1007/s11440-007-0027-y.
83. Issen, K.; Casey, T.; Dixon, D.; Richards, M.; Ingraham, J. Characterization and modeling of localized compaction in aluminum foam. *Scr. Mater.* **2005**, *52*, 911–915. https://doi.org/10.1016/j.scriptamat.2004.12.031.
84. Bastawros, A.; Bart-Smith, H.; Evans, A. Experimental analysis of deformation mechanisms in a closed-cell aluminum alloy foam. *J. Mech. Phys. Solids* **2000**, *48*, 301–322. https://doi.org/10.1016/S0022-5096(99)00035-6.
85. Park, C.; Nutt, S. Anisotropy and strain localization in steel foam. *Mat. Sci. Eng. A* **2001**, *299*, 68–74. https://doi.org/10.1016/S0921-5093(00)01418-0.
86. Papka, S.D.; Kyriakides, S. In-plane crushing of a polycarbonate honeycomb. *Int. J. Solids Struct.* **1998**, *35*, 239–267. https://doi.org/10.1016/S0020-7683(97)00062-0.
87. Eshelby, J.D. The determination of the elastic field of an ellipsoidal inclusion, and related problems. *Proc. R. Soc. Lond. A-Math. Phys. Eng. Sci.* **1957**, *241*, 376–396. https://doi.org/10.1098/rspa.1957.0133.
88. Katsman, R.; Aharonov, E.; Scher, H. Localized compaction in rocks: Eshelby's inclusion and the spring network model. *Geophys. Res. Lett.* **2006**, *33*. https://doi.org/10.1029/2005GL025628.
89. Katsman, R.; Aharonov, E.; Scher, H. A numerical study on localized volume reduction in elastic media: some insights on the mechanics of anticracks. *J. Geophys. Res. B* **2006**, *111*. https://doi.org/10.1029/2004JB003607.
90. Katsman, R.; Aharonov, E. A study of compaction bands originating from cracks, notches, and compacted defects. *J. Struct. Geol.* **2006**, *28*, 508–518. https://doi.org/10.1016/j.jsg.2005.12.007.
91. Thibodeau, S.; Alamdari, H.; Ziegler, D.P.; Fafard, M. New insight on the restructuring and breakage of particles during uniaxial confined compression tests on aggregates of petroleum coke. *Powder Technol.* **2014**, *253*, 757–768. https://doi.org/10.1016/j.powtec.2013.12.048.
92. Nguyen, H.N.; Prunier, F.; Djeran-Maigre, I.; Nicot, F. Kinetic energy and collapse of granular materials. *Granul. Matter* **2016**, *18*, 5. https://doi.org/10.1007/s10035-016-0609-1.
93. Nicot, F.; Sibille, L.; Darve, F. Failure in rate-independent granular materials as a bifurcation toward a dynamic regime. *Int. J. Plast.* **2012**, *29*, 136–154. https://doi.org/10.1016/j.ijplas.2011.08.002.
94. Hadda, N.; Nicot, F.; Bourrier, F.; Sibille, L.; Radjai, F.; Darve, F. Micromechanical analysis of second order work in granular media. *Granul. Matter* **2013**, *15*, 221–235. https://doi.org/10.1007/s10035-013-0402-3.
95. Holzapfel, A.G. *Nonlinear solid mechanics: A continuum approach for engineering*; John Wiley & Sons, Chichen., 2000. https://doi.org/10.1023/A:1020843529530.
96. Nicot, F.; Hadda, N.; Bourrier, F.; Sibille, L.; Wan, R.; Darve, F. Inertia effects as a possible missing link between micro and macro second-order work in granular media. *Int. J. Solids Struct.* **2012**, *49*, 1252–1258. https://doi.org/10.1016/j.ijsolstr.2012.02.005.
97. Basar, Y.; Weichert, D. *Nonlinear continuum mechanics of solids: fundamental mathematical and physical concepts*; Springer Science & Business Media, 2013. https://doi.org/10.1007/978-3-662-04299-1.
98. Cundall, P.A.; Strack, O.D. A discrete numerical model for granular assemblies. *Geotechnique* **1979**, *29*, 47–65. https://doi.org/10.1680/geot.1979.29.1.47.
99. Šmilauer, V.; Catalano, E.; Chareyre, B.; Dorofeenko, S.; Duriez, J.; Gladky, A.; Kozicki, J.; Modenese, C.; Scholtès, L.; Sibille, L.; others. Yade documentation. *The Yade Project* **2015**. http://yade-dem.org/doc/.
100. He, X.; Wu, W.; Cai, G.; Qi, J.; Kim, J.R.; Zhang, D.; Jiang, M. Work–energy analysis of granular assemblies validates and calibrates a constitutive model. *Granul. Matter* **2020**, *22*, 28. https://doi.org/10.1007/s10035-019-0990-7.
101. Nicot, F.; Lerbet, J.; Darve, F. Second-order work criterion: from material point to boundary value problems. *Acta Mech.* **2017**, *228*, 2483–2498. https://doi.org/10.1007/s00707-017-1844-1.
102. Stroeven, M.; Askes, H.; Sluys, L. Numerical determination of representative volumes for granular materials. *Comput. Methods Appl. Mech. Eng.* **2004**, *193*, 3221–3238. https://doi.org/10.1016/j.cma.2003.09.023.
103. Evesque, P.; Adjemian, F. Stress fluctuations and macroscopic stick-slip in granular materials. *Eur. Phys. J. E* **2002**, *9*, 253–259. https://doi.org/10.1140/epje/i2002-10082-4.
104. Catalano, E.; Chareyre, B.; Barthélemy, E. Pore-scale modeling of fluid-particles interaction and emerging poromechanical effects. *Int. J. Numer. Anal. Methods Geomech.* **2014**, *38*, 51–71. https://doi.org/10.1002/nag.2198.
105. Bagi, K. Stress and strain in granular assemblies. *Mech. Mater.* **1996**, *22*, 165–178. https://doi.org/10.1016/0167-6636(95)00044-5.
106. Bagi, K. Analysis of microstructural strain tensors for granular assemblies. *Int. J. Solids Struct.* **2006**, *43*, 3166–3184. https://doi.org/10.1016/j.ijsolstr.2005.07.016.
107. Zhu, H.; Nguyen, H.N.; Nicot, F.; Darve, F. On a common critical state in localized and diffuse failure modes. *J. Mech. Phys. Solids* **2016**, *95*, 112–131. https://doi.org/10.1016/j.jmps.2016.05.026.
108. Bardet, J.P. Numerical simulations of the incremental responses of idealized granular materials. *Int. J. Plast.* **1994**, *10*, 879–908. https://doi.org/10.1016/0749-6419(94)90019-1.
109. Tordesillas, A.; Pucilowski, S.; Sibille, L.; Nicot, F.; Darve, F. Multiscale characterisation of diffuse granular failure. *Philos. Mag.* **2012**, *92*, 4547–4587. https://doi.org/10.1080/14786435.2012.715766.
110. Das, A.; Tengattini, A.; Nguyen, G.D.; Viggiani, G.; Hall, S.A.; Einav, I. A thermomechanical constitutive model for cemented granular materials with quantifiable internal variables. Part II–validation and localization analysis. *J. Mech. Phys. Solids* **2014**, *70*, 382–405. https://doi.org/10.1016/j.jmps.2014.05.022.